Nitrogen-doped carbon-based single-atom Fe catalysts: Synthesis, properties, and applications in advanced oxidation processes

Yuxi Zeng[a,b,1], Eydhah Almatrafi[b,1], Wu Xia[a], Biao Song[a], Weiping Xiong[a], Min Cheng[a], Ziwei Wang[a], Yuntao Liang[a], Guangming Zeng[a,b*], Chengyun Zhou[a,b*]

[a]*College of Environmental Science and Engineering and Key Laboratory of Environmental Biology and Pollution Control (Ministry of Education), Hunan University, Changsha 410082, P.R. China*

[b]*Center of Research Excellence in Renewable Energy and Power Systems, Center of Excellence in Desalination Technology, Department of Mechanical Engineering, Faculty of Engineering-Rabigh, King Abdulaziz University, Jeddah 21589, Saudi Arabia.*

* Corresponding author at: College of Environmental Science and Engineering, Hunan University, Changsha, Hunan 410082, China.

Tel.: +86–731– 88822754; fax: +86–731–88823701.

E-mail address: zgming@hnu.edu.cn (G.M. Zeng), zhouchengyun@hnu.edu.cn (C.Y. Zhou). 1 These authors contribute equally to this article

Abstract

Single-atom catalysts (SACs) combine the benefits of both heterogeneous and homogeneous catalysts, they have emerged as the frontier in advanced oxidation processes (AOPs). The isolated active metal centers of carbon-based single-metal atom catalysts can be utilized to the maximum extent. They have recently gained popularity in the realm of environmental catalysis because of their high activity, selectivity, and structural/chemical stability. Nitrogen-doped carbon-based Single-atom Fe catalysts (Fe-SACs) have a high density of the active site, low metal leaching rate and good catalytic performance, and thus have attracted the attention of researchers. However, there seems to be a lack of thorough and critical reviews on the use of carbon-based Fe-SACs for AOPs degradation of organic water pollution. In this review, we focused on the Fe-SACs made of carbon-based materials and their synthesis methods and physical characteristics. We also investigated how Fe-SACs were used to effectively eliminate contaminants in different AOPs. In addition, the degradation mechanisms and stability of carbon-based Fe-SACs have been discussed. Finally, the advantages of carbon-based Fe-SACs in the catalytic degradation of pollutants are summarized, and the future opportunities and prospects of carbon-based Fe-SACs in the catalytic field are proposed.

Keywords: Single-atom Fe; Carbon-based; Environmental catalysis; Advanced oxidation processes; Organic pollutants

1. Introduction

With the ever-accelerated development of industrialization and urbanization, the rapid growth of the global population, the massive consumption of fossil fuels and climate change have brought increasingly serious environmental problems, posing great challenges to human health, environmental protection and energy demand [1-4]. More and more research is aimed at finding green, efficient and low-cost technologies to remove environmental pollutants [5-8]. Advanced oxidation processes (AOPs) can degrade refractory pollutants by generating highly reactive oxygen species (ROS) such as hydroxyl radical (HO·), sulfate radical($SO_4^{\cdot-}$), superoxide radical ($O_2^{\cdot-}$), and singlet oxygen ($^1O_2$), which has become a very popular environmental remediation process system [9-11].

Catalysts play a significant role in reducing production costs and improving reaction efficiency, which is widely used in the application of various environmental pollution control technology [12-14]. Depending on the phase of the reaction system, catalysts are usually divided into homogeneous catalysts and heterogeneous catalysts. Homogeneous catalysts have high activity and selectivity [15, 16]. By contrast, heterogeneous catalysts are more stable, and easier to be separated from the reaction system [17, 18]. In 2011, Prof. Tao Zhang and his team first proposed the concept of single-atom catalysts (SACs) [19]. In recent years, SACs have become a collaborative alternative to existing heterogeneous and homogeneous catalysts [20]. Single-atom catalysts are isolated single atoms dispersed over the carrier, which not only are able to maximize efficiency for the metal atoms, but also provide a more uniform and specific

active site than ordinary catalysts consisting of a variety of active sites [21, 22]. This enables SACs to play the role of homogeneous catalysts in local structure and catalytic performance [23, 24].

At present, varieties of supports have been reported for the synthesis of SACs. Among them, carbon carriers (e.g., graphene, N-doped porous carbon and Graphitic carbon nitride etc.) have become powerful carriers for the synthesis of stable metal atoms due to good graphite structure with high mechanical strength [25, 26]. Carbon-based materials rich in defect sites and heteroatoms have a large number of bond structures and coordination sites, which can strongly anchor metal atoms and effectively solve the problem of easy coalescence of metal atoms caused by high surface free energy. Therefore, the carbon-based single-atom catalysts have the advantages of low cost and high performance. Theoretically, the characteristics of SACs allow the maximum atomic utilization rate to be close to 100% [27]. Noble metal monatomic catalysts have long been used in heterogeneous catalysis [28, 29]. Compared with noble metal atomic catalysts, non-noble metal catalysts can reduce the cost and achieve similar performance to noble metal catalysts [30, 31]. Fe is cheap and abundant in nature, with high durability, and can be adjusted in acidic and alkaline media. Nitrogen-doped carbon-based single-atom Fe catalysts with atomic dispersion have excellent catalytic performance in oxygen reduction reactions and are the most promising non-noble metal catalysts to replace the noble metal catalyst [32, 33].

Many studies have reported the application of carbon-based single-atom Fe catalysts in the degradation of water environment in advanced oxidation processes, such

as some common types of organic pollutants: organic dyes (e.g., methylene blue [34, 35], methyl orange [36, 37], Acid Red 73 [38, 39], rhodamine B [40] etc.) and phenolic compounds (e.g., phenol [41, 42], bisphenol A [43, 44], p-nitrophenol [45, 46], p-chlorophenol [47, 48] and 2,4-dichlorophenol [49] etc.). In addition, Fe-SACs was used to catalytically accelerate the effective degradation of pharmaceuticals and personal care products (PPCPs) by AOPs. Currently, some common antibiotics (sulfamethoxazole [50, 51], tetracycline [52, 53], chloromycetin series antibiotics [54, 55] and quinolone antibiotics [56, 57]) and anti-inflammatory drug (paracetamol [58, 59] and diclorophenolic acid [60]) in water environments have been reported. Moreover, many single-atom Fe catalysts have been verified to be suitable and stable for the degradation of similar pollutants [61-63]. In recent years, the number of reviews on single-atom catalysts has gradually increased. Zhong et al. and Gao et al. mainly reviewed the application and working mechanism of SACs in photocatalysis [64, 65]. Lu et al. and Zhang et al. discussed the design of advanced battery systems using SACs and their applications in electro-catalysis [66, 67]. Gawande et al. reviewed the activities and applications of SACs in organic catalysis [21]. Huang et al.and Shang et al. described in detail the synthesis, characterization and application of SACs in water treatment by AOPs [68, 69].

However, it seems that there are few comprehensive reviews on the treatment of water organic pollution by single-atom Fe catalysts in AOPs. The review of Fe-based single-atom catalysts by Singh B's team focuses on electro-catalysis and electrochemical applications [27]. In this review, we summarize the different synthesis

strategies of carbon-based single-atom Fe catalysts in recent years, especially the steps and methods of preparing carbon-based Fe-SACs by pyrolysis with different precursors. Then we focus on its application in environmental catalysis, uncover the catalytic sites and related mechanisms of carbon-based Fe-SACs in different AOPs systems, and analyze the stability of different catalysts in the AOPs degradation system. Finally, the future development opportunities and research trends of Fe-SACs in the field of catalysis are discussed.

2. Synthesis of carbon-based Fe-SACs

The preparation of SACs requires the prevention of aggregation of metal atoms or the complete dispersion of concentrated nanoparticles. The SACs prepared in the past were of low metal load densities, and the synthesis of SACs is a significant challenge. In the synthesis of carbon-based Fe-SACs, the coordination unsaturated FeN_4 site anchored by four N atoms is the most common chemical species. The chemical states of single atomic metal sites can be determined and the presence of single-atom Fe (Fe-SA) can be confirmed using characterization techniques such as X-ray absorption near edge structure (XANES), high-angle annular dark field scanning transmission electron microscope (HAADF-STEM), and X-ray photoelectron spectroscopy (XPS), etc.

2.1 Pyrolysis

2.1.1 MOFs as the precursor

Metal-organic frameworks (MOFs) are three-dimensional ordered crystal

frameworks formed by bridging metal ions with ligands [70, 71]. Their three-dimensional (3D) molecular cage structure provides high specific surface area, porosity, thermal and chemical stability and abundant metal sites, making them ideal precursors for the preparation of SACs [72, 73].

Lin et al. synthesized catalysts with a single active center and high specific surface area through simple pyrolysis of MOFs precursors. The sample prepared at 900℃ showed single-atom properties, with 1.85 wt% Fe content in Fe50-N-C-900 SACs. The four pyrrole nitrogen sites in porphyrin-type MOFs can fix single metal atoms [74]. Jiao et al. designed a series of isomorphic MOFs (Fe_x-PCN-222) with ten one-dimensional middle channels with diameters of 3.2 nm by modulating the proportional modulation between Fe-TCPP (Tetra(4-carboxyphenyl)porphine) and H_2-TCPP mixed ligands. The 3D network of Fe_x-PCN-222 effectively inhibited iron aggregation during pyrolysis. The optimized Fe_x-PCN-222 can be converted into a single-atom Fe site for injection of porous N-doped carbon (Fe_{SA}-NC) after pyrolysis, giving it a specific mesoporous structure (Fig. 1a) [75]. In Fig. 1b, the high-resolution N 1s spectrum of Fe_{SA}-NC was fitted into five characteristic peaks. They correspond to pyridine N (398.5eV), Fe-N_x (399.2eV), pyrrole N (400.3eV), graphite N (401.2eV) and oxide N (402.7eV), respectively. In addition, there is no edge peak at about 7117.1eV, indicating that the symmetry of Fe-N_x sites in Fe_{SA}-NC was low (Fig. 1c). Fourier transform-extended X-ray absorption fine structure (FT-EXAFS) spectra showed only a main peak of Fe-N, and no Fe-Fe bond was detected (Fig. 1d), indicating that Fe in Fe_{SA}-NC was distributed as the single atoms, and an average of four nitrogen atoms were used to

coordinate each Fe atom (Fig. 1e).

Zeolitic imidazolate frameworks (ZIFs) are metal-organic frameworks (MOFs) material commonly used in the synthesis of SACs [69]. Zhang and his colleagues synthesized an iron-doped ZIFs precursor in the 20-1000nm range by bonding iron ions directly to imidazolate ligands in a 3D frame, and then obtained the atomic iron locations dispersed in porous carbon particles by one-step pyrolysis [76]. ZIFs provide N and C sources, Fe ions partially replace Zn, and imidazole ligands in iron form Fe-N_4 complex structure in the ZIF hydrocarbon network [70]. Li et al. confined the metallic precursor $Fe(acac)_3$ to a ZIF-8 cavity, forming isolated single-atom Fe (Fe-ISAs/CN) anchored to nitrogen species. The iron content in the catalyst is as high as 2.16 wt% [77]. Zhi and her colleagues prepared the dual-functional iron monatomic catalysts by pyrolyzing the coordination iron ions containing 2, 2-Bipy species. By coating graphene with polypyrrole (PPy) on both sides, they made it better able to immobilize ZIF-8 polyhedra with 2, 2-BiPy species of coordinated iron ions. Then after pyrolysis at 1000℃ and zinc sublimation, uniform single-center active FeN_x was obtained [41].

Bimetallic MOFs with other sacrificial metals can avoid metal center aggregation and carbon accumulation [73]. Chen et al. successfully synthesized Fe-SAs/CNF-900 from Zn-Fe bimetal ZIFs by pyrolysis. Under pyrolysis, the volatilization of Zn may leave some micropores and then form the Fe–N_x sites. The contents of Fe were determined to be 4.58 wt%, whereas the content of Zn was below 0.05 wt% [78]. Recently, zinc assisted atomization strategy has been developed to incorporate Fe and

Ni monatomic into MOF-derived nitrogen-doped carbon (Fe_1-Ni_1-N-C). The ZIF-8 can be converted into nitrogen-doped porous carbon. At the same time, the center metal Zn was vaporized in the pyrolysis process, and Fe and Ni were trapped by nitrogen doped carbon and formed the Fe_1-Ni_1-N-C catalysts [79].

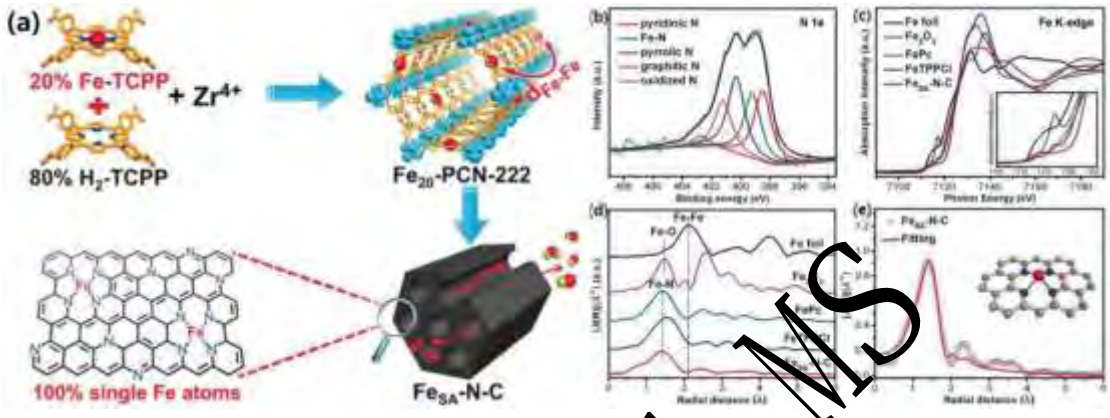

Fig. 1(a)Illustration of single Fe atoms-involved FeSA-N-C catalyst; (b) High-resolution XPS spectrum of N 1s for FeSA-N-C; (c) Fe K-edge X-ray absorption near-edge structure (XANES) ; (d) Fourier transform-extended X-ray absorption fine structure (FT-EXAFS) spectra; (e) EXAFS fitting for FeSA-N-C [75].

Pickling can effectively remove excess metal particles to prevent their aggregation and make the metal position on the MOFs carrier atomically dispersed. Wang et al. encapsulated Fe(II)-phthalocyanine (FePc) molecules into the cavity of ZIFs and formed the FePc-x@ZIF-8. FePc was used as the precursor of Fe and N, and the metal site density and carbon pore size can be adjusted by controlling the dosage of FePc. Excessive FePc polymolecular aggregation could include the Fe_2O_3. The additional metal species in Fe-SAs-N/C-x could be removed by acid leaching [80]. The iron precursor ammonium ferric citrate (AFC) was employed to anchor citrate ions on the surface of ZIF-8. They then prepared C-AFC©ZIF-8 with isolated Fe-N sites by pyrolysis and acid-leaching [81]. Citrate had a strong interaction with Fe(III) and strong coordination with Zn(II), so it was difficult to exchange ions between AFC and ZIF-8,

193 but some citrate ions could exchange ligands with 2-methylimidazole [82].

194 **2.1.2 Polymers as the precursor**

195 Metal atoms can be entirely dispersed by coordination with elements in C- and N-
196 rich polymer precursors [83]. Du et al. prepared a layered porous iron monatomic
197 catalyst (Fe-NC-SAC) on N-doped carbon using Fe salts, polyvinylpyrrolidone (PVP)
198 and melamine as precursors. The iron content in Fe-NC-SAC was 1.5 wt%. The PVP
199 can limit the recrystallization of ferric salts. The ferric salts can act as self-templates to
200 generate graded pores and form the Fe-N_x sites [84]. Guo et al. prepared a catalyst for
201 g-C_3N_4 embedding monoatomic iron sites by pyrolysis of Fe-imidazole coordination
202 compound (Fe-ICC) and melamine (MA) (Fig. 2a). The g-C_3N_4 has homogeneous N
203 atoms and a "sixfold cavity," which can stabilize high-density single-atom areas. By
204 calculating the Fe binding energies of different N configurations in g-C_3N_4 (Fig. 2b), it
205 was found that the single-atom Fe strongly tended to move towards the center [85]. In
206 another report, $Fe(NO_3)_3 \cdot 9H_2O$, MA and thiourea (TU) were used as the raw ingredients
207 in a sulfur-assisted method to create a cellular Fe/g-C_3N_4 catalyst [35]. In order to get
208 more fully dispersed Fe species, S was regarded as a "sacrificial carrier" and finally
209 escapes in the form of SO_2 with the pyrolysis process.

210 Du et al. synthesized Fe-SA catalysts in the presence of dicyandiamide, glucose
211 and ferric chloride by pyrolysis in the Ar atmosphere. The peaks such as Fe^0 and iron
212 oxide were not observed in the X-Ray Diffraction (XRD) spectrum of Fe-SA, Fe doping
213 would produce more defect sites on the surface of carbon materials [86]. Xiong et al.

first coordinated dicyandiamide with Fe salts to form a coordination polymer and calcinated in an argon atmosphere. Then the catalyst was reduced by hydrogen to form the SAS-Fe catalyst which has a metal load of up to 30 wt% [87]. Due to the ease of preparation and amplification of Fe coordination polymers, the resulting SAS-Fe can be synthesized at a gram grade. The aberration-corrected HAADF-STEM images observed that all iron species existed in a single atomic position, and no clusters or sub-nanoparticles were detected. This synthesis strategy proved to be universal and has been successfully extended to other metal precursors, and corresponding SAS catalysts could also be synthesized in gram grade.

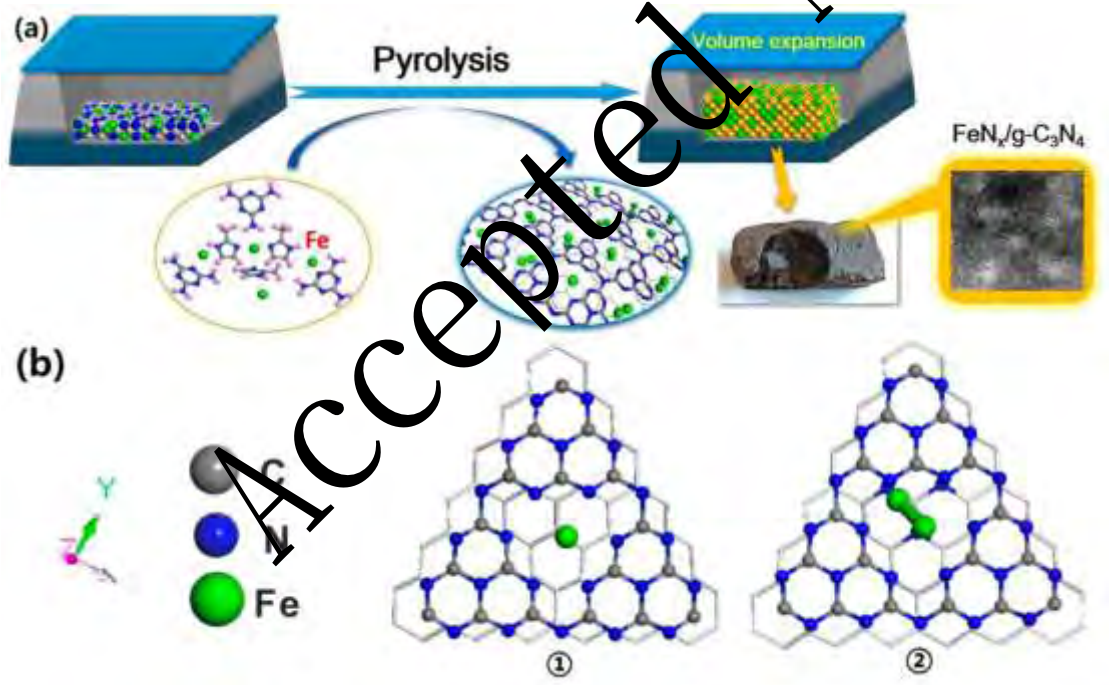

Fig. 2(a)Pyrolytic synthesis of $FeN_x/g\text{-}C_3N_4$ catalysts; (b)Optimized structures of various positions of single-atom Fe in $g\text{-}C_3N_4$, (①) single-atom Fe in the center of 6-fold cavity, (②) single-atom Fe in interlayer [85].

2.1.3. Small organic molecules as the precursor

It has been proved that nitrogen-rich organic small molecules can be directly used

as carbon and nitrogen precursors to prepare SACs at a low cost [88]. Yang et al. synthesized Fe-SACs using the iron cation complexed with 1, 10-phenanthroline onto commercial carbon black in an argon atmosphereat 600℃ . This synthesis strategy has also been proved to synthesize multicomponent metal SACs. For example, Fe/Co-SACs, Ru/Fe-SACs and other bimetallic SACs have been successfully synthesized [89]. In addition, chelating agents effectively isolate metal ions, allowing them to be attached to the carbon skeleton. Zhao et al. reported a method for synthesizing multiple Fe-NC SAC with metal loads up to 12.1 wt% by a cascade anchor strategy. The Fe-NC SAC with only one maximum strength of about 4.5 $Å^{-1}$ by wavelet transform (WT) analysis. It was very similar to that of FePc, but unlike Fe foil. The Fe-NC SAC synthesized by this method has an iron content of 8.9 wt%, and this strategy can be used for low-cost mass production of Fe-NC SAC [90].

Wang et al. reported an in situ Fe doping method using direct pyrolysis to synthesize a 2D Fe/N co-doped carbon network. Melamine was added to the mixed solution of $FeCl_3$ and 1,10-phenanthroline (PT) chloride under high-temperature treatment under argon gas flow. Then the black powder obtained was washed with H_2SO_4 acid leaching and pyrolyzed again to obtain the final Fe-NC-PT catalyst (Fig. 3a). The ligands with bisnitrogen-containing groups (bis-NCGs) attached to PT were used as "crab clips" (Fig. 3b), which effectively coordinated the Fe ions to extend the spatial barrier and inhibit heterogeneous growth. The folded carbon nanonetworks in g-FeNC-PT samples could construct layered porous structures with a large surface area and promote the rapid transfer of carbon surfaces. The HAADF-STEM image (Fig. 3c)

confirmed the presence of many fully dispersed single-atom Fe in the sample. The element mapping image (Fig. 3d) verifies that Fe and N elements were evenly distributed in the nanonetworks. This method has a higher yield, fewer synthesis steps and lower cost than the template method [91].

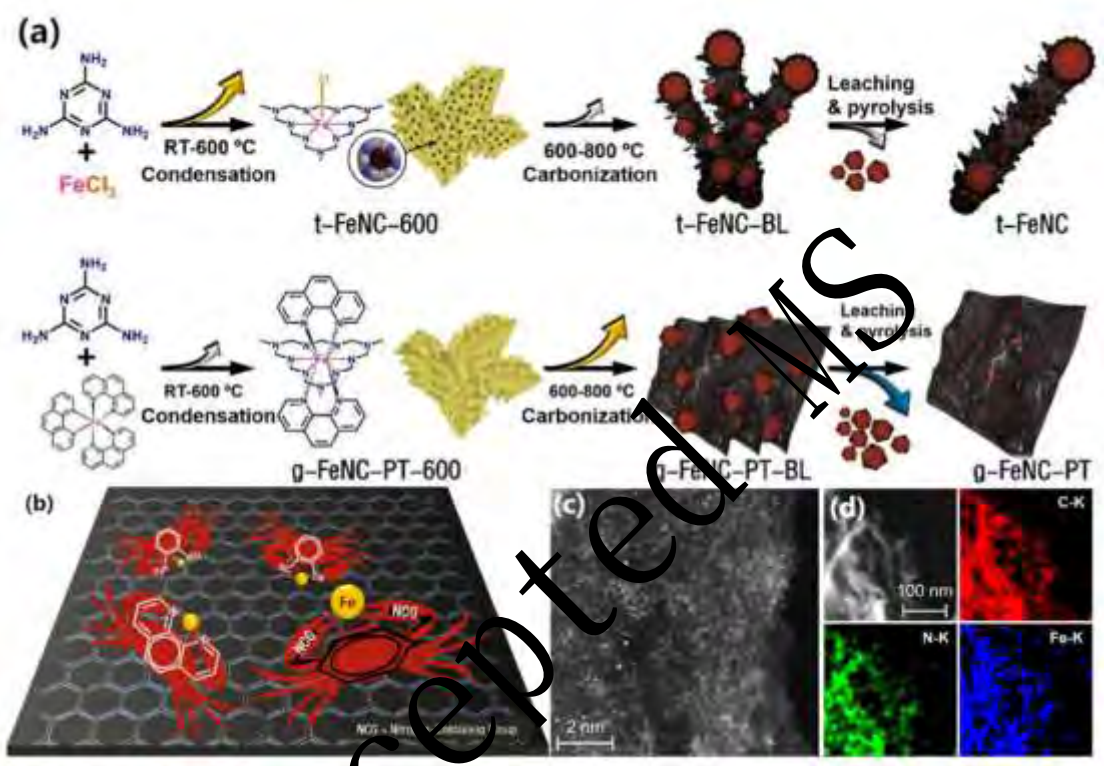

Fig. 3(a)Sketch for the preparation of Fe-NC-PT; (b) Illustration of the Coordination of Bis-NCG with Iron Ions; (c) HAADF-STEM image ; (d) corresponding element mapping images for C (red), N (green), and Fe (blue) of Fe-NC-PT [91].

2.1.4. Biomass as the precursors

The functional groups (such as -OH and -COOH) in biomass can stabilize metal ions, prevent metal ions from aggregating during carbonization, and well restrict metal atoms in carbon matrix [92-94]. The iron content in biomass is not high and well dispersed, which is conducive to the expansion of the distance between adjacent atoms, thus promoting the formation of isolated atoms in high-temperature pyrolysis reactions

265 so biomass can be used as precursors to synthesize SACs [95, 96].

266 *Enteromorpha* is green algae rich in nitrogen compounds, such as polysaccharides,
267 proteins and vitamins. What's more, *Enteromorpha* is rich in iron. Chen et al.
268 carbonized *Enteromorpha prolifera* in the N_2 atmosphere at 500℃ to obtain
269 *Enteromorpha* biomass, then mixed with KOH and pyrolyzed in situ at 600-900℃ in
270 argon atmosphere, and co-doped into carbon-containing materials to obtain Fe-N@C-
271 x (Fig. 4a). The scanning electron microscope (SEM) image (Fig. 4b) showed the
272 inherent porous structure of FeN@C700, and the SEM element diagram (Fig. 4c)
273 showed that N corresponds to C distribution and Fe dispersed in the structure. The
274 transmission electron microscope (TEM) images (Fig. 4d, e) showed the presence of
275 nanosheets in the carbon layer of Fe-N@C700, and the crystal spacing was similar to
276 that of graphite. The TEM element diagram (Fig. 4f) indicated that N and Fe inherent
277 in *Enteromorpha* were co-doped after pyrolysis. The team also used the same process
278 to produce metal-free catalysts for other nitrogen-rich biomass (soybeans, spirulina,
279 beanstalk and kelp) [58]. Similarly, Peng et al. prepared Fe-N-C catalyst by direct
280 pyrolysis of *Enteromorpha*, and observed Fe clusters and atom-dispersed FeN_x sites
281 derived from inherent Fe in *Enteromorpha*. All the Fe sites in its configuration were
282 dispersed in the carbon framework as a single-atom Fe and existed in the form of Fe-N
283 bonds [59].

284 In another report, *Spirulina* was used as an N, S co-doped Fe source by Lei et al.
285 to prepare a single-atom Fe site binding ultra-small Fe_2O_3 nanoclusters embedded in N,
286 S co-doped porous carbon (Fe_{SA}/FeO_{NC}/NSC) through in-situ transformation strategy.

287 In the Fe_{SA}/FeO_{NC}/NSC structure, Fe-Fe bonds are few, Fe-N and Fe-O bonds coexist,
288 and there are apparent FeN_4 active centers [97]. *Auricularia Auricular-Judae* (AAJ)
289 was also a good source of N and Fe atoms. Wang et al. synthesized dispersed single-
290 atom Fe anchored to nitrogen-doped carbon by using renewable AAJ as a precursor
291 without an external iron source. In the synthesis process, they cleverly mixed urea and
292 AAJ, and the mixture decomposed simultaneously to increase the content of nitrogen
293 doping and active center [98]. The *Myriophyllum aquaticum* plants have abundant
294 porous structures, and they were transformed into biochar by Li et al. to prepare a
295 catalyst of Fe single atoms [42].
296 Lotus root-derived hydrogels were used by Chen et al. as a starting precursor for
297 production of 3D porous carbon aerogel-supported SACs. Microporous defects in the
298 gel can capture and stabilize a single iron atom. During the in-situ creation of
299 microporous defects, a single iron atom is captured and stabilized in NCA_{LR}/Fe,
300 forming a highly active FeN_4 catalytic center [99]. Many other biomass precursors have
301 been used to prepare single-atom Fe catalysts. Zhang et al. used heme chloride (a six-
302 coordinate iron porphyrin compound with Cl ligand) as a natural Fe source and laver
303 as biochar, prepared an N-doped graded porous carbon (NHPC) supported single-atom
304 Fe catalyst (SA-Fe/NHPC) by pyrolysis at 800℃ in an argon atmosphere. The mass
305 content of iron was 2.3wt% [100]. In addition, biomass waste was also expected to be
306 utilized. Li et al. successfully prepared a number of high-performance Fe-SACs through
307 simple pyrolysis of Fe-contaminated biomass ferns collected from forests [57].

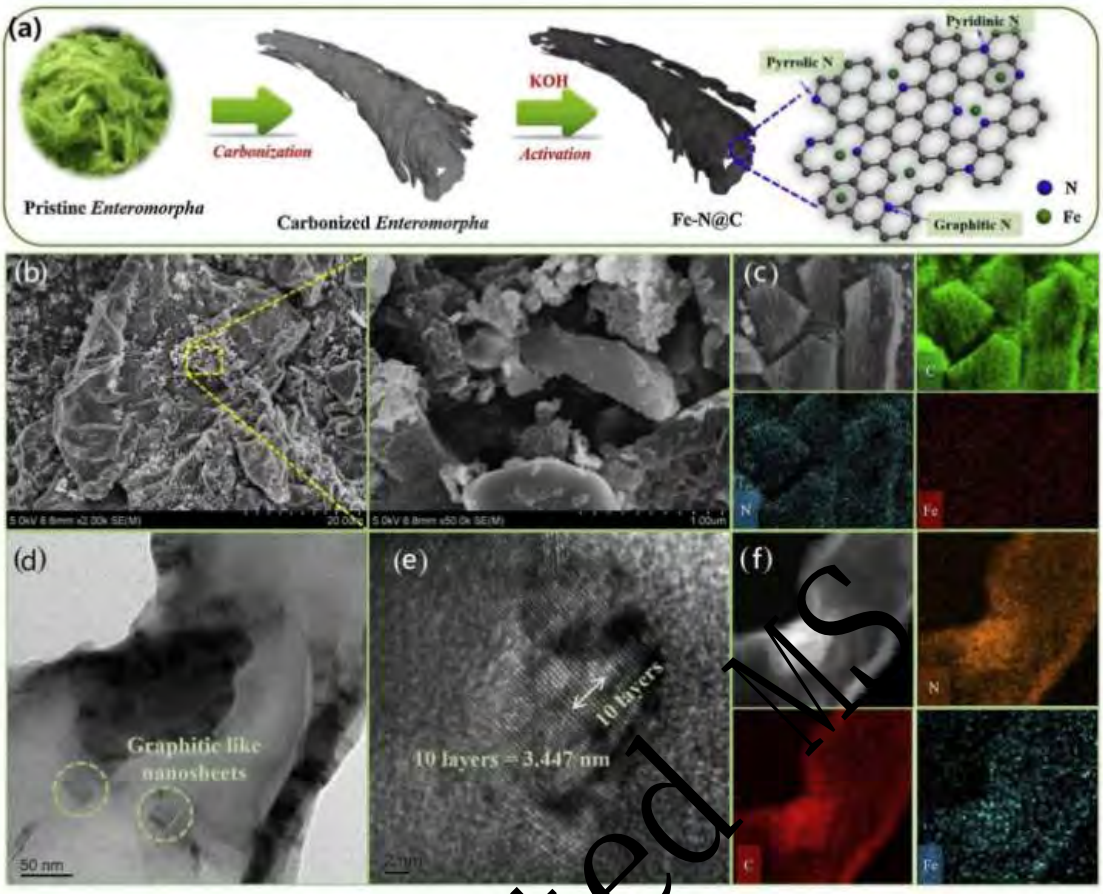

Fig. 4(a)preparation scheme of Fe-C@N from the Enteromorpha biomass; (b) SEM of Fe-N@C 700 (c) SEM element mappings of Fe-N@C 700; (d) TEM of Fe-N@C 700 (50 nm); (e) TEM of Fe-N@C 700 (2 nm); (f) TEM element mappings of Fe-N@C 700 [58].

2.2. Wet impregnation

The wet impregnation method is a simple and effective method for synthesizing SACs by implanting single metal atoms on a carbon matrix. Wet impregnation generally consists of two steps, first, introducing the metal precursor into the prefabricated carrier material through impregnation at different pH values and temperatures, and then adjusting the properties through subsequent treatment steps (reduction or oxidation treatment) [101, 102].

Huang et al. assembled 3D graphene hydrogels by mixing graphene oxide (GO), metal precursors and H_2O_2, then hydrothermally treated the resulting suspension. After

lyophilization, the gel was thermally annealed in a NH_3 atmosphere to obtain a series of N-doped porous graphene frames (M-NHGFs, M=Fe, Co or Ni). Individually metal atoms were introduced into the binding sites of the graphene lattice. The MN_4C_4 part adopts the same coordination environment, and the stable valence stated of metal in Fe-NHGF was Fe(III) [103]. By using a sequential impregnation technique, Yang et al. synthesized N-doped acid-treated carbon (NAC) supported Ni-Fe catalysts. These catalysts have Fe oxides, Ni oxides, Fe^0, N species and FeN_x on the surface, Where Fe^0 only appears at 4Ni2Fe@20NAC [36]. In addition, Wang et al. synthesized magnetic carbon-coated Fe-C/N composites using g-C_3N_4 and $FeC_2O_4{\cdot}2H_2O$ as raw materials by simple impregnation method and then calcination in the N_2 atmosphere. The major ingredients of Fe-C/N-0.5:1 were Fe_3N and Fe_3C, and its shell was nitrogen-doped carbon [39]. Jiang et al. impregnated ferrous acetate and 1, 10-phenomena into ethanol, stirred it to make ethanol evaporate, and then ground and calcined the obtained solid to obtain Fe-N-C containing monatomic Fe(III), with an iron content of about 5.0 wt% [49].

A large number of oxygen functional groups in materials such as go and carbon nanotubes capture and absorb metal ions. To stabilize the atom-dispersed Fe sites, Zuo et al. created a sandwich structure using g-C_3N_4 and reduced graphene oxide (rGO) [53]. The rGO was mixed with deionized water under magnetic agitation, and dicyandiamide (DCD) was then connected to the GO layer. Adding the rGO layer improves the stability of atom-dispersed Fe on g-C_3N_4 substrate because of the formation of additional Fe-O bonds between Fe and rGO. The holes mostly stayed on the rGO layer, which would

significantly improve the photocatalytic activity of atomic metal positions in C_3N_4-Fe-rGO composites compared with that in C_3N_4-Fe.

2.3. Physical and chemical deposition

SACs formation can be achieved by depositing atomic material onto selected supporting substrates, such as atomic layer deposition (ALD) and chemical vapor deposition (CVD). ALD is considered a powerful physicochemical vapor deposition method for preparing SACs, it can precisely control the production of various thin films at the atomic level, which contains the size of catalysts [104, 105]. Wang et al. deposited uniform dispersed single iron atoms on multi-walled carbon nanotubes (MWCNTs) by controlling the dose and time as well as the number of Fe-ALD cycles, with Fe loading up to 0.36 wt%. During the reaction process, nitrogen flushing was used to remove unreacted precursors and by-products, and N_2 purge was added after ferrocene and H_2 were put in during the coating cycle. After ten Fe ALD cycles, it can be seen that individual Fe atoms scatter on multi-walled carbon nanotubes [106].

The CVD technique is widely used in preparing two-dimensional materials due to its precise control of material structure and purity. The CVD growth process of 2D materials can be adjusted by controlling parameters such as precursor, substrate, pressure and temperature [107]. Wang et al. synthesized single atom Fe-N_4-PC materials by vapor deposition (CVD). As shown in Fig. 5a, Fe-Pc was added to pyridine to dissolve as a precursor of Fe and then bubbled into a CVD system filled with $Mg(OH)_2$ templates. Large diameter $Mg(OH)_2$ templates and iron oxide were removed

by H_2SO_4 solution, the resulting material was washed with ethanol and deionized water and then pyrolyzed to obtain the final monatomic Fe-N_4-PC. The Fe-N_4-PC has a thin layer of graphitized carbon structure with abundant mesopore, and Fe fixed to the carbon material has a weight percentage of 1.23 wt%. In Fig. 5b, the Fe foil's wavelet transform (WT) contour map showed a maximum intensity Fe-Fe signal at about 77.8$Å^{-1}$. In contrast, Fe-N_4-PC only showed a maximum intensity value related to Fe-N bonds at about 4$Å^{-1}$ (Fig. 5c), further proving the atomic dispersion of Fe atoms [50].

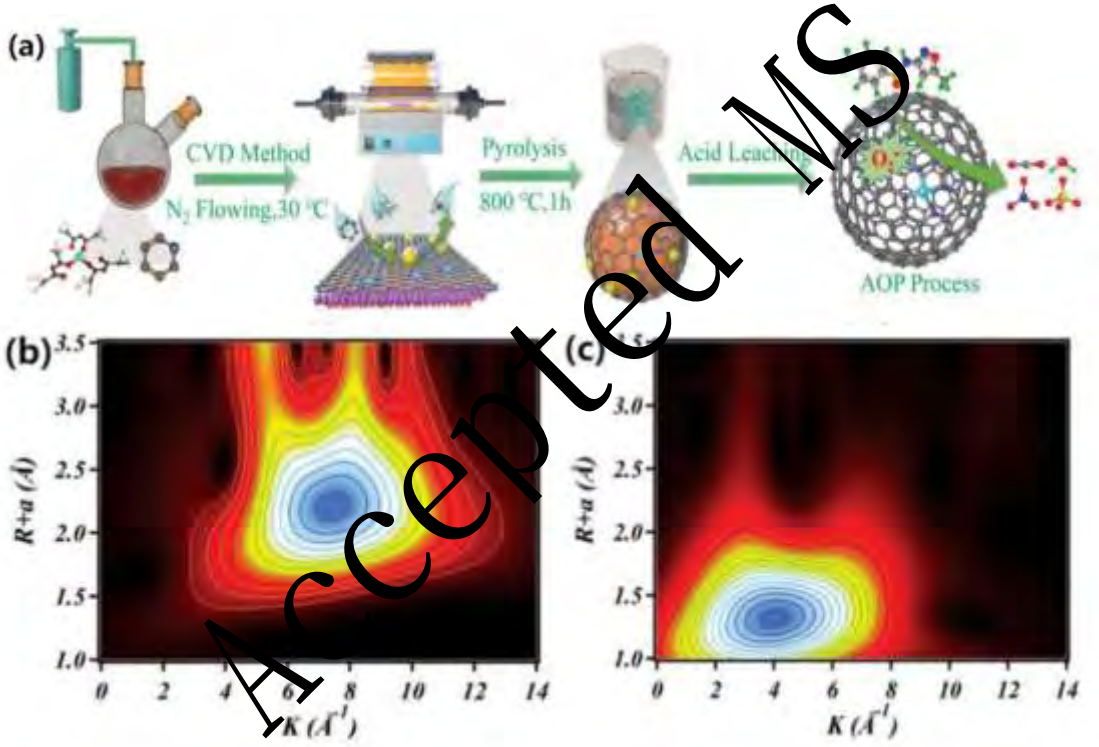

Fig. 5(a)Schematic for the synthesis of Fe-N_4-PC materials; WT of the Fe K-edge (b)Fe foil and (c)Fe-N_4-PC [50].

2.4. Ball-milling method

High-energy ball milling has proven to be a powerful method of cutting and reconstructing materials, effectively breaking and rebuilding chemical bonds due to the high mechanical energy input. Therefore, ball milling is also a standard method of

preparing SACs [108, 109]. Guo et al., successfully prepared the Fe atoms dispersed on SiO_2 (Fe©SiO_2) by high-energy ball milling of Fe_2SiO_4 with SiO_2 [110]. The method is simple operation, and the size of SACs can be well controlled by adjusting the rotational speed of the ball.

Bao and his colleagues prepared a series of graphene-embedded FeN_4 catalysts (CUS-FeN_4/GN) with different iron content by ball-milling ferrous phthalocyanine (FePc) and graphene nanosheet (GN). A highly dispersed Single center of FeN_4 was obtained, in which the coordination unsaturated iron center was largely confined to the graphene matrix. The adjacent carbon atoms of FeN_4 could be further reconstructed under the high energy of ball milling, resulting in the formation of FeN_4 embedded into the center of the graphene matrix. However, in the high-energy ball milling process, defects would be introduced into the graphene net around some Fe atoms, resulting in some disordered structures in the high-resolution transmission electron microscopy (HRTEM) image simulated by DFT [111]. Qian et al. constructed the FeN_4 structure on the carbon nanotube (CNT) by ball milling of Fe-C_3N_4 and carbon nanotube mixture, then calcination at different temperatures in the N_2 atmosphere, and obtained the single atom catalyst (Fe_{SA}-N-CNT). Fe-C_3N_4 was obtained by calcination of a mixture of $Fe(acac)_3$ and $C_2H_4N_4$ with a uniform distribution of Fe doping positions (Fig. 6a). The HRTEM images (Fig. 6b) showed that the surface of Fe_{SA}-N-CNT was covered with a large amount of nitrogen-doped carbon, and no Fe^0 particles were observed. The HAADF-STEM (Fig. 6c) can be marked in many iron monoatomic sizes. As shown in Fig. 6d, Fe and N are well-dispersed in the C-N fused layer. Fe content in Fe_{SA}-N-CNT

400 was as high as 6.08 wt%, and most single atoms were exposed to the catalyst surface
401 [112].

402 Peng et al. used g-C_3N_4 as the carrier and Fe-ICC as the precursor to create Fe-
403 SACs. Fe was successfully embedded into g-C_3N_4, and Fe-g-C_3N_4(600) obtained the
404 highest Fe content of 4.07 wt%. By DFT calculation, the isolated Fe atom in g-C_3N_4
405 tended to occupy the quadruple coordination doped configuration, and its formation
406 energy was 2.794 eV [52]. Moreover, FeN_4/GN composites synthesized by ball milling
407 Fe phthalocyanine and graphene nanosheets have highly dispersed coordination
408 unsaturated Fe sites, which Cui et al. used to prepare dye-sensitized solar cells. The
409 single iron active site is confined to the graphene plane and has good stability and
410 electro-catalytic activity [108]. Similarly, Chen et al. prepared some FeN_4/GN catalysts
411 that showed higher oxygen reduction reaction (ORR) activity when Fe content was 2.7
412 wt% [109]

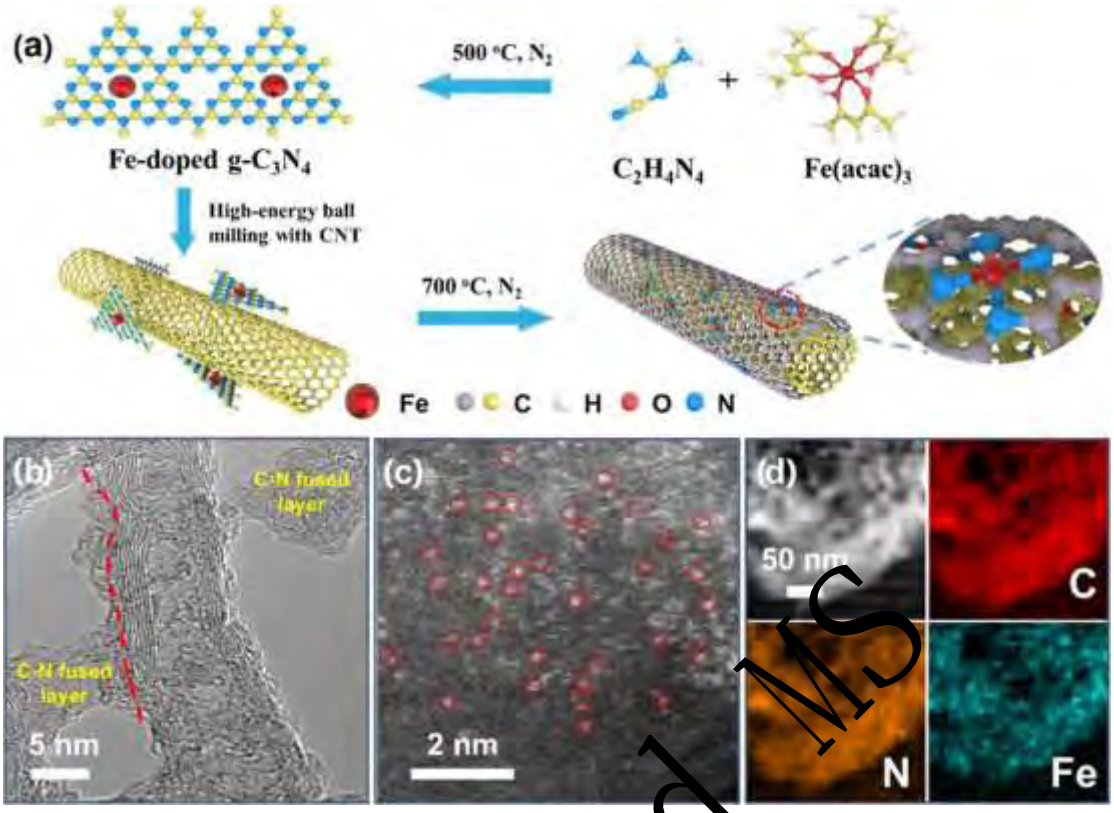

Fig. 6(a) Illustration of the fabrication procedure of a Fe_{SA}-N-CNT catalyst via a high-energy ball milling and two-step isolation synthesis method; (b) high-resolution transmission electron microscopy (HRTEM) image; (c) high-angle annular dark-field scanning transmission electron microscopy (HAADF-STEM) image; (d) energy-dispersive X-ray (EDX) mappings of the Fe_{SA}-N-CNT sample. [112].

Table 1 summarizes the preparation methods of the above mentioned carbon-based Fe single-atom catalysts, including the pyrolysis of multiple carriers, wet impregnation, physical and chemical deposition, ball milling, etc. In practical engineering applications, the production cost, operation difficulty and whether it can be mass-produced should be considered. The synthesis of Fe-SACs by wet impregnation method is rapid and easy to operate. However, the materials prepared by this method often have low metal loading and the risk of secondary contamination caused by residual solvent. In the process of preparing SACs by ALD and CVD, the metal size can be accurately controlled, but this method has high requirements on experimental equipment and low yield. Ball milling method is suitable for large-scale preparation without waste liquid,

but it has high energy consumption and high noise. In addition, the above methods also have some limitations in the selection of carbon-based materials. In contrast, among the existing synthesis techniques, pyrolysis strategy is the most common method used to prepare SACs. This method is low cost, requires simple treatment of the precursors, and can even be directly pyrolyzed in a one-pot process. In addition, new metal coordination is generated during pyrolysis, and the loading and structure of the material can be controlled by adjusting the precursor composition and pyrolysis temperature. However, high temperature will promote the aggregation of metal atoms, so the problem of material load should be considered when using pyrolysis method.

Table 1

Summary of the various carbon-based Fe-SACs for preparation methods

Catalyst	Carbon-support	synthesis methods	Fe loading	Ref
Fe-ISAs/CN	NPC	ZIF-8 and $Fe(acac)_3$, pyrolysis (900℃)	2.16 wt%	[77]
Fe_{50}-N-C-900	NPC	Fe-ZIF-8, pyrolysis (900℃)	1.85 at%	[74]
Fe_{SA}-NC	NPC	FeTCPP-MOF, pyrolysis(800℃)	1.76 wt%	[75]
Fe-SAs/CNF-900	NPC	$Zn_{20}Fe_1$-ZIF, pyrolysis (900℃)	4.58 wt%	[78]
Fe_1-Ni_1-N-C	NPC	Fe&Ni-ZnO/ZIF-8, pyrolysis	0.45 wt%	[79]
Fe SAs-N/C-20	NPC	ZIF-8 and FePc, pyrolysis (900℃)	0.20 wt%	[80]
C-AFC©ZIF-8	NPC	ZIF-8 and AFC, pyrolysis (900℃)	0.64 wt%	[81]
FeN_x-PNC	NPC	Ppy-coated graphene-ZIF-8, pyrolysis (1000℃)	0.86 at%	[113]
Fe-NC SAC	NPC	$Fe(NO)_3$, PVP and MA, pyrolysis (900℃)	1.50 wt%	[114]
I-FeN_x/g-C_3N_4-x	g-C_3N_4	Fe-ICC and MA, pyrolysis (600℃)	18.2 wt%	[85]
S-Fe-salt/CN	g-C_3N_4	$Fe(NO_3)_3$, MA and thiourea, pyrolysis (600℃)	17.1 wt%	[35]
FeSA-NC	NPC	$FeCl_3$, dicyandiamide and glucose, pyrolysis (900℃)	2.45 wt%	[86]
SAS-Fe	NPC	$Fe(NO_3)_3$ and dicyandiamide-formaldehyde resin, pyrolysis (600℃)	30.0 wt%	[87]
Fe-SACs	Carbon black	Complexing metal and 1,10-phenanthroline, pyrolysis (600℃)	1.85 wt%	[89]
FeNC-PT	g-C_3N_4	$FeCl_3$, MA and PT hydrochloride, pyrolysis (800℃)	1.1 at %	[91]
Fe-NHGFs	NG	Impregnation of $FeCl_3$,pyrolysis (900℃)	0.05 at%	[103]
Fe-C/N-0.5:1	g-C_3N_4	Impregnation of FeC_2O_4, pyrolysis (550℃)	(-)	[39]
4Ni2Fe@20NAC	NAC	Impregnation of $Fe(NO_3)_3$, $Ni(NO_3)_2$, pyrolysis (500℃)	2.26 wt%	[36]
Fe-N-C	NPC	ferrous acetate and 1,10-phenanthroline, pyrolysis (700℃)	5.0 wt%	[49]
C_3N_4-Fe-rGO	NG	$FeCl_3$ and dicyandiamide, pyrolysis (550℃)	5.0 wt%	[53]
Fe-N@C	Biochar	Carbonized-Enteromorpha, pyrolysis (900℃)	0.6 wt%	[58]

Fe-N-C	Biochar	Dry and crush enteromorpha, pyrolysis (900℃)	0.84 wt%	[59]
Fe-ISA/NC	Biochar	Auricularia auricular-judae and urea, pyrolysis (1000℃)	0.026 wt%	[98]
Fe_{SA}/FeO_{NC}/NSC	Biochar	Carbonized spirulina, NH_4Cl and urea, pyrolysis (900℃)	0.25 wt%	[97]
ISA-Fe/MC	Biochar	Myriophyllum aquaticum and K_2FeO_4, pyrolysis (800℃)	2.4 wt%	[42]
NCA_{ST}/Fe	Biochar	lotus root powders, $FeCl_2$ and MA, pyrolysis (950℃)	1.3 wt%	[99]
SA-Fe/NHPC	Biochar	heme chloride and dimethylformamide, pyrolysis (800℃)	2.3 wt%	[100]
FeSAC-800	Biochar	Fe-contaminated biomass waste ferns, pyrolysis (800℃)	(-)	[57]
FeN_4/GN	NG	ball milling of FePc and graphene nanosheets	1.5 wt%	[111]
Fe_{SA}-N-CNT	CNT	ball milling of $Fe(acac)_3$, $C_2H_4N_4$ and carbon nanotube	6.08 wt%	[112]
Fe-g-C_3N_4(600)	g-C_3N_4	ball milling of 2-MI, PVP and $FeSO_4·7H_2O$	4.07 wt%	[52]
FeN_4/GN	NG	ball milling of FePc and graphene nanosheets composites	2.7 wt%	[115]
Fe/MWCNTs	CNT	Fe $(Cp)_2$ and multiwalled CNT; atomic layer deposition	0.36 wt%	[106]
Fe-N_4-PC	NPC	Iron (III) acetylacetonate, pyridine; chemical vapor deposition	1.23 wt%	[50]

Fe-PC = iron(II) phthalocyanine, NG = N-doped graphene, GO=graphene oxide, NPC = N-doped porous carbon, AFC=ammonium ferric citrate, MA=melamine, Fe-ICC=Fe-imidazole coordination compound, PVP=Polyvinylpyrrolidone; PPy=polypyrrole; NAC=N-doped acid-treated carbon, CNT=carbon nanotube; 2-MI=2-methylimidazole

3. Applications in advanced oxidation processes

Despite the relatively low loading of most metals in carbon-based Fe-SACs, they could also exhibit good catalytic effects compared to conventional heterogeneous catalysts. In photocatalytic system, single-atom Fe catalysts could improve light absorption and shorten electron transfer distances through interactions with ligands. In Fenton system, atomically dispersed Fe-N_x sites could promote organic adsorption and hydrogen peroxide-activated redox reactions. Fe-based SACs could catalyze the formation of ·OH from H_2O_2 and degrade organic pollutants. In activated persulfate (PMS and PDS) systems, organic pollutants could be degraded by two different pathways: free radicals (HO·, $SO_4·^-$ and $O_2·^-$) and non-free radical ($^1O_2$, Fe(IV)═O and Fe(V)═O). Table 2 summarizes all the single-atom Fe catalysts for the degradation of organics in advanced oxidation processes mentioned in this paper.

3.1. Photocatalysis

Photocatalysis is considered to be the process of reducing and oxidizing reactions by which a catalyst absorbs photons with the generation of high-energy electrons and holes. Photocatalytic reactions involve three main reaction steps: light harvesting, charge generation and separation, and catalysis [116-118]. In general, the introduction of a single-atom into the optical carrier capture may change the structure of the energy carrier and electronic structure, thus regulating the optical absorption behavior and charge transfer dynamics [119].

Liu et al. tested the photocatalytic activity of N-doped graphene nanosheets of iron clusters (Fe-NG/MCNS) as catalysts and found that the Fe-NG/MCNS promoted the degradation of antibiotics, endocrine disruptors and dyes well [37]. Tonda's team investigated the effect of Fe-doped g-C_3N_4 photo-catalysts on the photocatalytic activity of rhodamine B (Rh B) degradation [45]. The degree of Fe doping has a significant impact on the photocatalytic degradation of Rh B, and Fe-doped g-C_3N_4 exhibits extremely effective photocatalytic activity. ·OH was formed during the photocatalytic oxidation process, but $O_2^{\cdot-}$ was an important free radical in the degradation of Rh B. Under sunlight, the photo-generated electrons excited in the conduction band (CB) of g-C_3N_4 were captured by Fe(III) species, reducing the existing electron receptor O_2 to $O_2^{\cdot-}$. Similarly, Youngtak Oh et al. investigated the photocatalytic function of the divalent Fe atom-coordinated g-C_3N_4 system (Fe-g-C_3N_4). Under light, Fe-g-C_3N_4 has a substantially better photocatalytic activity for p-nitrophenol (PNP) than g-C_3N_4, indicating that divalent Fe atom can be used as electron

and hole capture sites to enhance photo-generated excitons separation [120].

Fe-based integrated SACs photo/PMS systems have been used for the removal of pollutants. Li et al. prepared a series of Fe-SACs from biomass waste and applied it for antibiotics removal. Aided by peroxymonosulfates (PMS), Fe-SACs showed excellent photocatalytic degradation efficiency of norfloxacin (NOR). In Fig. 7a showed the band gap energy (E_g) of catalysts. Fe-SAC-800 had the narrowest band gap in the sample (Fig. 7b), which is favorable for light harvesting in photocatalytic reactions. The Fe-SAC-800 sample had the highest photocurrent density (Fig. 7c) and the lowest electron transfer resistance, which resulted in a better charge transfer efficiency. Moreover, the Fe-SAC-800 catalyst showed good degradation of five other quinolone antibiotics, with the presence of multiple reactive oxygen species (ROS) in the degradation reaction system, including $SO_4^{\cdot-}$, ·OH, $O_2^{\cdot-}$ and $^1O_2$ [37]. The degradation mechanism (Fig. 7d) mainly includes three steps: (1) the effective activation of PMS to form Fe(IV)═O (Eq. 1-5), while the activated Fe-SACs produced electrons and holes (Eq. (6)); (2) the formation of active species: $O_2^{\cdot-}$ (Eq. (7)), $^1O_2$ (Eq. (8)), ·OH (Eq. (9)), $SO_4^{\cdot-}$ (Eq. (10)-(11)); (3) the reaction of the reactive species with NOR molecules, resulting in degradation (Eq. (12)).

$$FeSAC + HSO_5^- \rightarrow Fe(\text{III}) + SO_4\cdot^- + HO^- \quad (1)$$

$$FeSAC + HSO_5^- \rightarrow Fe(\text{III}) + \cdot OH + SO_4^{2-} \quad (2)$$

$$Fe(\text{III}) + HSO_4^- + H_2O \rightarrow [Fe(\text{III})OOSO_3]^+ + H^+ \quad (3)$$

$$[Fe(\text{III})OOSO_3]^+ \rightarrow Fe(\text{IV}) = O + SO_4^{2-} \quad (4)$$

$$Fe(\text{IV}) = O + NOR \rightarrow Fe(\text{III}) + products \quad (5)$$

499 $FeSAC + h\nu \rightarrow FeSAC\,(e^- + h^+)$ (6)

500 $O_2 + e^- \rightarrow \cdot O_2^-$ (7) $\cdot O_2^- + h^+ \rightarrow {}^1O_2$ (8)

501 $\cdot O_2^- + e^- + 2H^+ \rightarrow H_2O_2 + e^- \rightarrow HO^- + \cdot OH$ (9)

502 $\cdot OH + SO_4^{2-} \rightarrow SO_4 \cdot^- + HO^-$ (10)

503 $2SO_5 \cdot^- \rightarrow {}^1O_2 + 2SO_4 \cdot^-$ (11)

504 $(SO_4 \cdot^-, \cdot OH, O_2 \cdot^- \text{ and } {}^1O_2) + NOR \rightarrow products$ (12)

505 There have been many reports that carbon-based SACs have been employed to
506 degrade organic contaminants via the photo/H_2O_2 reactions. The Fe-doped g-C_3N_4
507 nanosheets synthesized by Gao et al. showed the best methylene blue (MB) degradation
508 under visible light irradiation with FeCNS-0.5 photocatalysts containing 0.5% Fe, as
509 well as the maximum photocatalytic activity for Rh B degradation catalytic activity. It
510 photodegraded at a rate 1.4 times faster than pure g-C_3N_4 nanosheets and 1.7 times
511 faster than bulk g-C_3N_4 nanosheets [34]. An et al. used I-FeN_x/g-C_3N_4-5 with an iron
512 loading of 18.2wt%, which showed excellent activity when organic contaminants were
513 degraded by photo/H_2O_2 reactions. Several common organic pollutants could be
514 completely eliminated in 15 minutes at neutral pH. These can be attributed to the large
515 number of Fe(II)-N_x active sites in I-FeN_x/g-C_3N_4, which can quickly activate H_2O_2 to
516 create HO· radicals [85]. In another report by Guo's group, during advanced oxidation,
517 S-Fe-salt/CN catalysts with atomically scattered Fe sites showed high activity in the
518 breakdown of several organic contaminants. In particular, the addition of S-Fe/CN-4 to
519 H_2O_2 under visible light irradiation showed an efficient removal rate of methyl bromide
520 close to 100% within 5 min. Moreover, all other S-Fe-salt/CN catalysts were able to

completely remove MB within 25 min, which fully reflects the effectiveness of the S-assist [35].

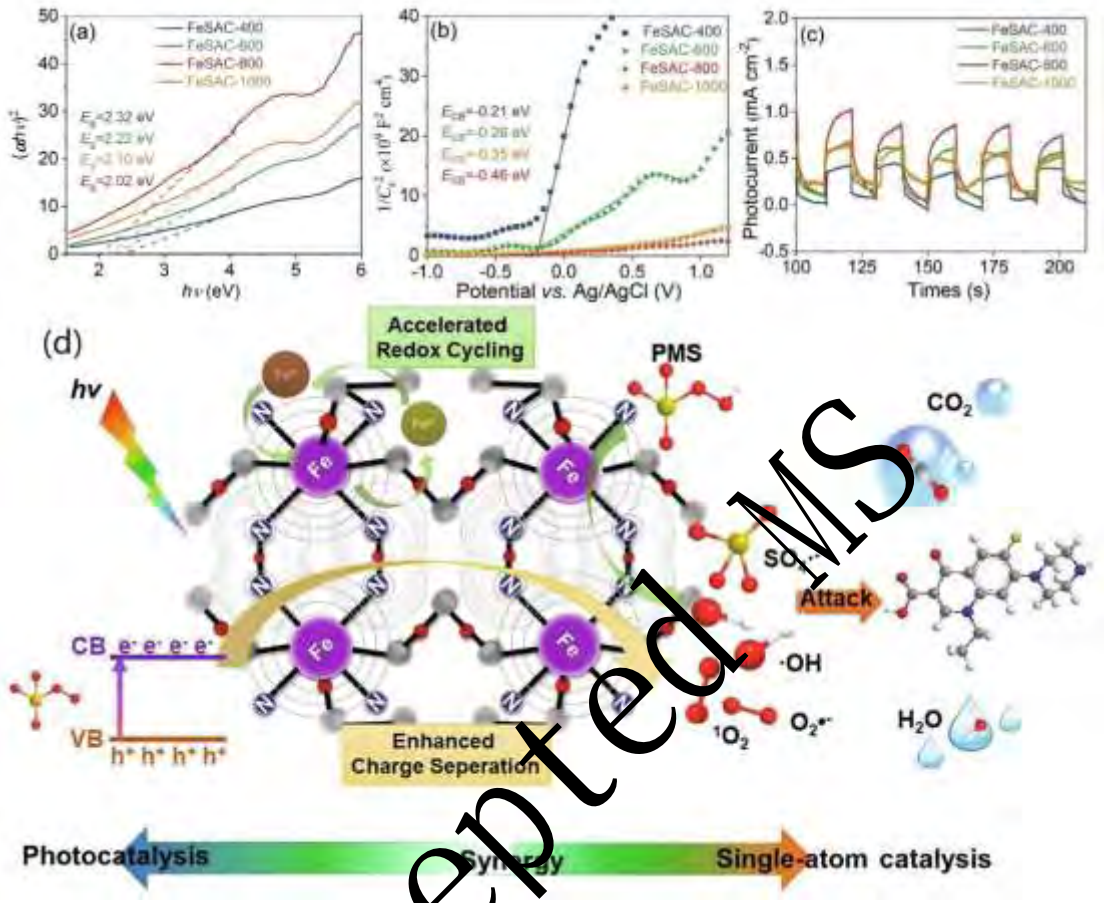

Fig.7 (a) UV-vis DRS spectra Tauc's plots; (b) Mott-Schottky plots; (c) Transient photocurrent responses; (d)Proposed mechanism for the photodegradation of NOR on FeSAC-800 [57].

Photocatalytic activation of O_2/O_3 to create reactive substances for the breakdown of organic contaminants was carried out using g-C_3N_4 catalysts that were doped with Fe. Cao et al. used single-atom Fe/g-C_3N_4 in solar photocatalytic systems for water treatment. Apparently, Fe-g-C_3N_4 was more active than g-C_3N_4 in the photocatalytic ozonation of oxalic acid (OA), with 4.5 Fe-g-C_3N_4 exhibiting the best performance, removing 100 percent of OA within 30 min, compared to 39.3% OA degradation by g-C_3N_4. Fe doping accelerated the transfer of electrons to the oxygen adsorbate and increased the number of photogenerated electrons and their capacity for reduction, in

534 which different sizes or coordination numbers of Fe sites have a distinct influence on
535 activation capacities for O_2/O_3. The fraction of photogenerated electrons was controlled
536 by the presence of Fe nanoparticles in visible light involved in the ozone, double and
537 triple electronic reduction approach (Eq. (13)), which reduced the percentage of the
538 single electron pathway, increasing the rate of ·OH production (Eq. (14-15)), and
539 improving the visible light electron reduction activity and the stability of ozone (O_3)
540 [121].

541 $$O_2 \xrightarrow{e^-} HO_2 \cdot / \cdot O_2^- \xrightarrow{e^-} H_2O_2 \xrightarrow{e^-} \cdot OH \quad (13)$$

542 $$O_3 \xrightarrow{e^-} \cdot O_3^- / HO_3 \cdot \rightarrow \cdot OH \quad (14)$$

543 $$O_2 \xrightarrow{e^-} \cdot O_2^- \xrightarrow{O_3} \cdot OH \quad (15)$$

544 **3.2. Catalyzing Fenton reactions**

545 The Fenton reaction produces highly reactive hydroxyl radicals (·OH) from H_2O_2
546 [122, 123]. Compared to other oxidants, H_2O_2 is low-cost and environmentally friendly
547 without causing secondary pollution problems [124]. The traditional heterogeneous
548 Fenton reaction was characterized by slow Fe(II) formation, high H_2O_2 consumption
549 and reacted under acidic conditions. The single-atom catalyst was expected to show the
550 highest Fenton/Fenton-like reactions due to their high molecular utilization rate [125,
551 126].

552 Carbon-based single iron atom catalysts have been reported to activate H_2O_2 over
553 a wide pH range. Ma et al. produced a catalyst (Fe-g-C_3N_4/GMC) that activated H_2O_2
554 over a wide pH range (4-10). Within 40 min, Fe-g-C_3N_4/GMC achieved 99.2% removal

555 of AR73, which was more efficient than that of g-C_3N_4 and Fe-g-C_3N_4 [38]. Moreover,
556 Fe-g-C_3N_4/GMC also showed good removal of Rh B, 4-CP, BPA and other pollutants.
557 H_2O_2 first formed a precursor surface complex with Fe(III)-N, which was then
558 reversibly decomposed into Fe(II)-N and ·OH, triggering the REDOX cycle of
559 Fe(II)/Fe(III) and the formation of ·OH [127]. The key active site for the successful
560 activation of H_2O_2 was the well-dispersed Fe-N_x in Fe-g-C_3N_4/GMC, and the π-π
561 stacking of GMC could greatly facilitate the reaction induced by Fe(III).
562 Meanwhile, ·OH preferentially degrades the organic matter adsorbed on the catalyst's
563 near-surface, avoiding the influence of OH^- [38]. Su et al. reported a SACs(Fe_1-NV/CN)
564 that formed a highly concentrated electron density at the Fe site. The Fe_1-
565 N_V/CN/H_2O_2/Vis system could remove 91% of ciprofloxacin (CIP) in 60 min, which
566 was 18 times more effective than the original CN degradation under the same conditions
567 [128]. Mu et al. prepared a catalyst (U-g-PAO/Fe) with an Fe(III) content of 24.04 wt%,
568 where the amidoxime moiety chelated the Fe(III) ions without causing them to
569 aggregate. U-g-PAO/Fe degraded 99.94% ofloxacin (OFX) in 35 min under H_2O_2 and
570 visible light. Furthermore, the chelated Fe(III) was stable under extreme conditions and
571 changes in the pH range of 2-10 had little effect on OFX degradation. The ·OH radicals
572 were the decisive radical for OFX degradation in H_2O_2/DMPO/U-g-PAO/Fe system
573 [62].

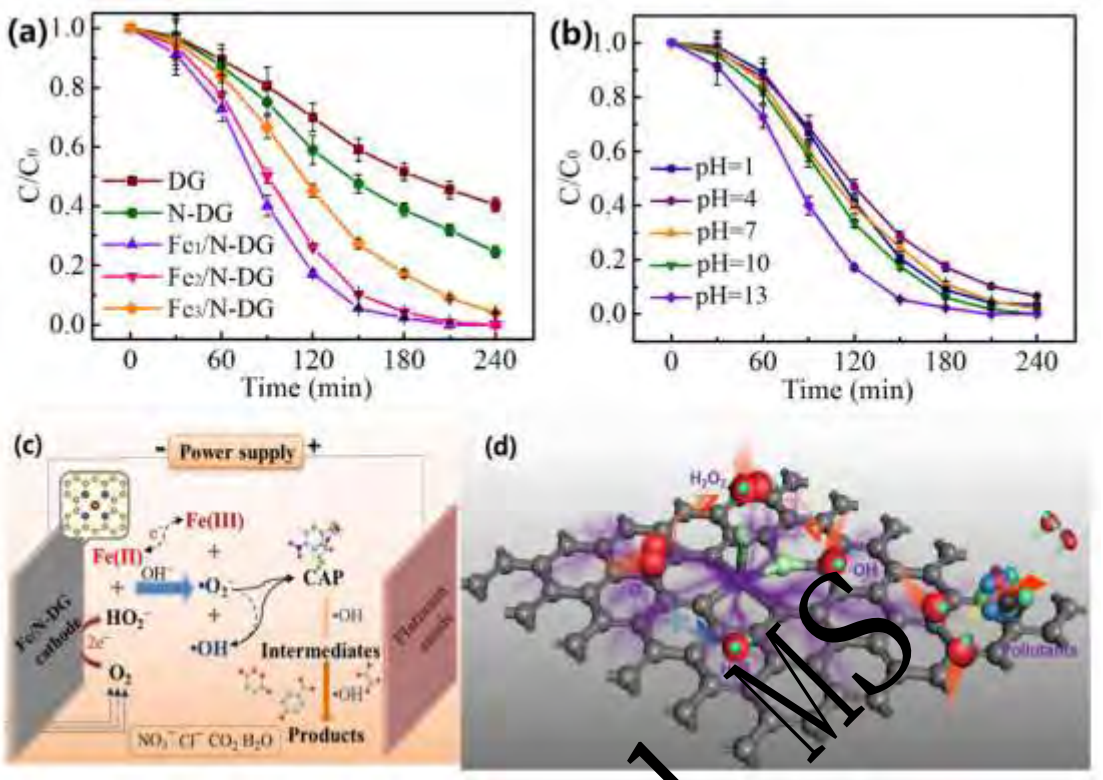

Fig. 8(a) Effect of different catalysts; (b) initial pH value on CAP removal; (c)Schematic illustrations of in situ H_2O_2 production and CAP removal [55]. (d) Formation of surface-bound HO· species on the 3D porous carbon structure of AD-Fe/$_3$DPC [46].

In general, electro-Fenton can only be utilized in acidic solutions (pH-3). In neutral solutions, the degradation efficiency is low due to Fe ion precipitation [129]. Single-atom Fe catalysts also break the application limits of narrow pH values in electro-Fenton technology, and even show good catalytic performance under extreme pH conditions. Zhang et al. designed a dual-function electro-Fenton catalyst (SAFe@HSC) with the morphology and hollow structure of a sea urchin. O_2 was effectively electrocatalyzed to H_2O_2 and rapidly generated ·OH over a wide pH range of 3-11, which showed good removal of the thiamphenicol (TAP) [54]. For the degradation of chloramphenicol (CAP), Song et al. used an iron-anchored N-DG catalyst (Fe/N-DG) as the cathode material to further convert the produced H_2O_2 molecules into free radicals [55]. In Fig. 8a, the cathodes containing Fe atoms were significantly more

589 efficient in the degradation of CAP than DG and N-DG. The H_2O_2 generated by oxygen
590 reduction at the cathode surface played a key role. It is worth mentioning that both
591 extreme pH values, resulted in CAP clearance of over 90% in less than 180 min (Fig.
592 8b). Under alkaline circumstances, through self-decomposition of H_2O_2 and oxidation
593 of Fe(II) by H_2O_2 (HO_2^-, when pH>11.7) (Eq. (16)), free radicals, ·OH and $\cdot O_2^-$, could
594 be produced on the surface of the Fe/N-DG cathode (Eq. (17-18)). Those free radicals
595 then attack the CAP, forming intermediates that are eventually converted completely
596 into small inorganic molecules, as shown in Fig. 8c

597 $$O_2 + H_2O + 2e^- \rightarrow HO_2^- + OH^- \quad (16)$$

598 $$H_2O_2 + HO_2^- \rightarrow \cdot OH + \cdot O_2^- + H_2O \quad (17)$$

599 $$Fe(\mathrm{II}) + 2HO_2^- \rightarrow Fe(\mathrm{III}) + \cdot OH + \cdot O_2^- + OH^- \quad (18)$$

600 When the unique unsaturated coordination environment interacts with the single-
601 atom iron-based catalyst, the mass activity of the electro-Fenton system to produce ·OH
602 is significantly enhanced. Cao et al. immobilized dispersed iron atoms on a 3D porous
603 carbon carrier (AD-Fe/3DPC) and proposed that in the electro-Fenton oxidative
604 degradation of sulfamethoxazole (SMX) system [46]. Surface ·OH exhibits exceptional
605 selectivity for the oxidation of three different organic compounds, benzoic acid, phenol
606 and nitrobenzene, was demonstrated by tests in ring-neutral solutions. The "selective
607 oxidation" characteristics of surface-bound HO· were largely related to the charged
608 features and electron density distribution of the target pollutant. At isolated Fe sites in
609 unsaturated coordination of C and Cl, H_2O_2 molecules can be successfully activated to
610 adsorb on the C_3-Fe-Cl_2 active center. The structure of AD-Fe/3DPC (Fig. 8d) can be

loaded with more dispersed Fe sites, improving its catalytic performance. Zhao et al. designed a Fe/Cu bi-metallic monoatomic catalyst (FeCuSA-NPC) for the electro-Fenton process, which could effectively decompose and mineralize chlorine-containing pollutants [63]. On a single-atom Cu, the chlorinated contaminants were dechlorinated. Then O_2 adsorbed on porous carbon was reduced to H_2O_2 through the double-electron ORR pathway, which was then decomposed by monatomic Fe into ·OH radical. The FeCuSA-NPC electro-Fenton process could remove 4-CP in the pH range of 3-9. Moreover, FeCuSA-NPC degraded chlorinated organic pollutants with a mass activity of 545.1-1374 $min^{-1}g_{metal-1}$, which exceeded the maximum value reported by electro-catalyst.

3.3. PMS activation

Compared with traditional ·OH radicals, $SO_4^{\cdot-}$ showed a higher oxidation potential and a wider pH range for effective reactions with organic compounds [130]. Most commonly, $SO_4^{\cdot-}$ is produced by activating peroxomonosulfate (PMS) or persulfate (PS) [131, 132]. Compared to PS, PMS can be effectively activated by transition metals to generate $SO_4^{\cdot-}$ due to its asymmetric molecular structure [133]. Persulfate-based AOPs activated by PMS produce powerful reactive oxygen species (ROS), such as free radicals ($HO\cdot$,$SO_4^{\cdot-}$ and $O_2^{\cdot-}$) and singlet oxygen ($^1O_2$) [134], which can effectively mineralize refractory organic compounds through both free radical and non-free radical pathways [135, 136].

By co-doping N and Fe atoms, nitrogen coordination Fe (Fe-N_x) is created, which

632 can change the electronic structure of the Fe-N-C catalyst's surface and greatly enhance
633 its conductivity and catalytic activity. [137]. In Fe-doped carbon-based monatomic
634 catalysts, the Fe-N_x site has thus been proposed as the main active site for PMS
635 activation. [138]. He and colleagues created Fe-N-C catalysts using Fe@ZIF precursors,
636 which increased the number of Fe-Nx sites. Under the equal conditions, the 1.2Fe-N-C
637 activated PMS with the highest amount of Fe-doping showed the best removal
638 efficiency of phenol, which is sufficient to indicate that Fe-N_x is the main active center
639 for accelerating the oxidation reaction. Additionally, 1.2Fe-N-C/PMS was selective in
640 the oxidation of various refractory organic compounds. Rh B, phenol, 4-CP, BPA and
641 TC were effectively degraded by the rapid oxidation in a non-free radical pathway
642 through $^1O_2$ [43]. As an alternative to MOF, covalent organic skeleton (COF), a new
643 carbon-nitrogen rich precursor. Yao et al. successfully prepared SAC-Fe (Fe@COF)
644 embedded in COF, and the doped Fe formed an effective single-atom Fe-N_x active
645 center preferentially in the carbon skeleton, successfully activating PMS to produce $^1O_2$
646 [139]. In the report of Wang et al., single atomic Fe-N-C materials had good organic
647 adsorption capacity and could efficiently degrade SMX by activating PMS. The
648 introduction of Fe single atoms not only greatly improved the catalytic activity of
649 carbon catalyst, but also tuned the activation pathway of PMS. In the activation process
650 of PMS, the bonded N in the Fe-N_4-C structure enhances the adsorption of organic
651 molecules by the material, while the single-atom Fe activates PMS to generate $O_2^{\cdot-}$
652 radical, thus transforming the activation pathway of PMS from a non-radical to a radical
653 process [50]. Similarly, with $^1O_2$ as the main ROS, the degradation of p-nitrophenol

(PNP) by single-atom Fe showed good catalytic performance with high TOC removal rate and high conversion frequency (TOF) reported by Du and his colleagues [86]. $^1O_2$ could be formed by self-decomposition of PMS (Eq. (19)) or by conversion of $O_2^{\cdot -}$ radicals during PMS activation (Eq. (20)).

$$HSO_5^- + SO_5^{2-} \rightarrow HSO_4^- + SO_4^{2-} + {}^1O_2 \quad (19)$$

$$2O_2^{\cdot -} + 2H_2O \rightarrow H_2O_2 + HO^- + {}^1O_2 \quad (20)$$

Li et al. prepared an isolated Fe-SACs (ISA-Fe/MC) deposited on *Myriophyllum aquaticum*-based biochar, which showed significantly superior catalytic performance compared with nano-Fe/MC [42]. In the PMS system, ISA-Fe/MC could completely eliminate phenol within 6 min, and the degradation rate constant (k) was 1.096 min^{-1}, while the k value of phenol degradation by nano-Fe/MC was 0.033 min^{-1}, an enhancement of about 33.2-fold. In the nano-Fe/MC/PMS system, the oxidation of phenol was caused by the free radical pathway dominated by $SO_4^{\cdot -}$, While in the ISA Fe/MC/PMS system, the oxidation of phenol was brought on by an electron transfer-dominated non-free radical route, and C-Fe was considered as the main electron transfer bridge. Moreover, ISA-Fe/MC was also effective in degrading BPA, SD and HBA. Chen et al obtained Fe-N@C from pyrolysis of *Enteromorpha* biomass for the degradation of paracetamol (PCM) in the aquatic environment [58]. In all Fe-N@C/PMS systems, PCM was completely removed, and the higher the pyrolysis temperature, the more PCM was eliminated from Fe-N@C catalysts due to their higher graphite N fraction (%). Similarly, $O_2^{\cdot -}$ was very crucial in PCM degradation and the non-free radical pathway ($^1O_2$) was dominant in the Fe-N@C/PMS system.

Additionally, the breakdown of PCM was significantly aided by the transmission of electrons between PMS, PCM molecules, and catalyst surfaces.

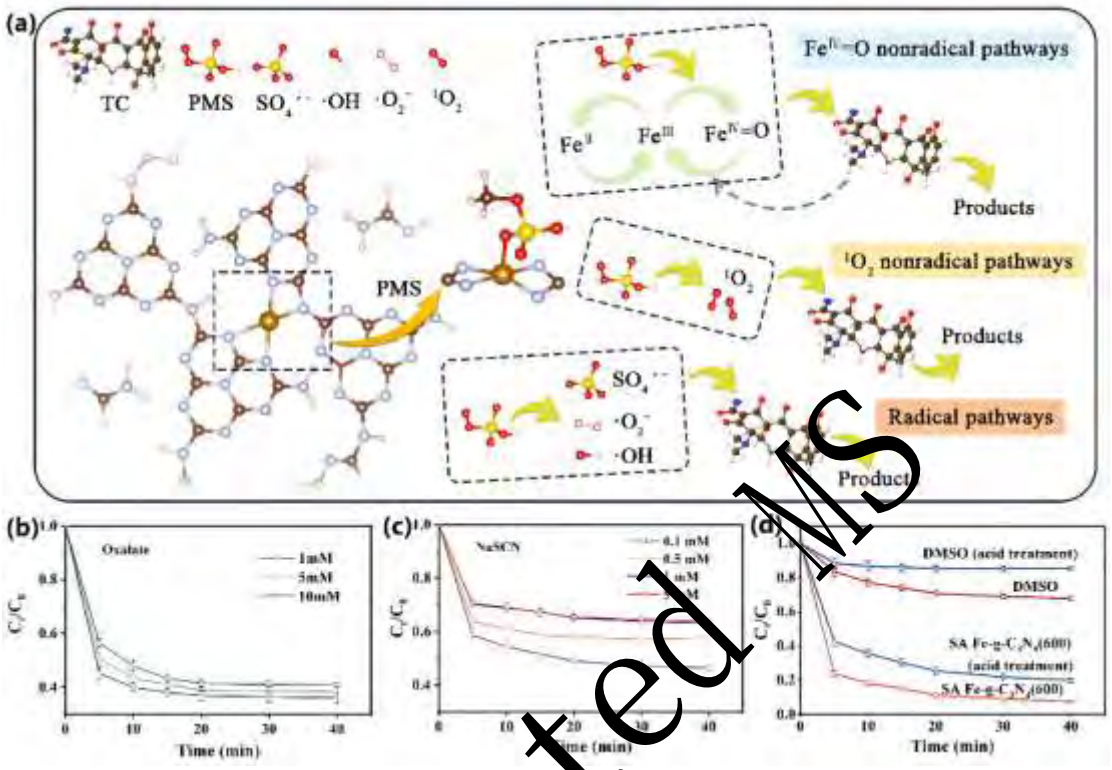

Fig. 9 (a) The proposed mechanism for the Fenton-like reactions in the SA Fe-g-C_3N_4 (600)/PMS system; (b, c)The effects of oxalate and citrate on TC degradation by SA Fe-g-C_3N_4/PMS system; (d) the catalytic performance of SA Fe-g-C_3N_4 (600) after hot acid treatment and the quenching effect by DMSO [52].

High-valent iron-oxo species (Fe(IV)═O and Fe(V)═O), which can function as the principal ROS to breakdown contaminants in a non-radical way, can be formed when PMS oxidizes Fe-based single atomic materials. In the PMS activation system mediated by Fe(III)-tetraamide macrocyclic ligand ($Fe^{(III)}$-TAML) designed by Li et al., the resulting high-valent iron oxygen complex ($Fe^{(IV)}$(O)TAML) can effectively degrade 4-CP in wastewater through the electron transfer pathway [48]. Similarly, Fe(III)-doped g-C_3N_4 (CNF) was employed by one team to degrade 4-CP and as a catalyst to activate PMS. The coordination Fe (III) in g-C_3N_4 served as the primary site of 4-CP degradation, and the primary reactants were the high-valent iron-oxo species

produced by PMS activation. The initial valence state of the Fe center in the Fe coordination complex was used to determine the valence state of the high-valence iron-oxo species [47]. Peng et al. used a Fe-based single-atom catalyst (SA-Fe-g-C_3N_4) as PMS activator to catalyze the oxidation of tetracycline (TC) [52]. The higher the pyrolysis temperature, the more Fe-N_4 sites of catalyst were obtained, and the better the catalytic performance. The quenching experiments proved that in the SA Fe-g-C_3N_4/PMS system for the degradation of TC, $SO_4^{\cdot-}$ and ·OH contributed little, $O_2^{\cdot-}$ radical played a certain role, and the non-radical process of $^1O_2$ contributed more. TC catalytic oxidation process is shown in Fig. 9a. To block the Fe sites, oxalate and NaSCN can create metal carboxyl complexes. When they were added to the system, they showed a strong quenching reaction and TC degradation was significantly inhibited (Fig. 9bc). Acid etching removed most of the iron clusters from the catalyst surface and DMSO could act as a probe for the Fe(IV) reaction to produce $DMSO_2$. The degradation of TC by the catalytic system was only slightly reduced by the addition of hot acid treatment, while the degradation performance was significantly reduced by DMSO quenching (Fig. 9d). This suggested that the degradation of TC proceeded via a non-radical pathway, with the single-atom Fe being the main active site and Fe(IV)═O playing a major role. To create the Fe(III)$OOSO_3$ complexes, the Fe(III) type in the atom-dispersed Fe-N_4 site might coordinate with the O atom in the PMS (Eq. (21)). Then, Fe(III)$OOSO_3$ complex formed Fe(IV)═O by hetero-cleaving the O-O (Eq. (22)). The produced Fe(IV)═O may be transformed back to Fe(III) via the electron transfer step when the neighboring CT adsorbed at the N location was oxidized (Eq. (23)).

713 $$\equiv Fe(III) + HSO_5^- \rightarrow [Fe(III)OO\,SO_3]^+ + H^+ \quad (21)$$

714 $$[Fe(III)OO\,SO_3]^+ \rightarrow \equiv Fe(IV) = O + SO_4^{\cdot-} \quad (22)$$

715 $$\equiv Fe(IV) = O + TC \rightarrow products + \equiv Fe(III) \quad (23)$$

716 Apart from the above studies, some bimetallic SACs have reportedly demonstrated
717 superior catalytic performance to monometallic catalysts. Yang et al. described that in
718 FeCo@NC-1 catalysts, isolated diatomic metal nitrogen sites ($FeCoN_6$) make electron
719 transport much easier, which activated PMS [44]. It provided an overwhelming
720 advantage over the single metals Fe@NC and Co@NC for the degradation of BPA. 100%
721 degradation of BPA was achieved within 1 min for the FeCo@NC-1 sample with a first-
722 order rate constant (k) of 6.062 min^{-1}. Furthermore, the double reaction sites in
723 FeCo@NC-1 could also enhance the reaction by minimizing the migration distance
724 between the reactive radicals and the target pollutant. With the help of this research,
725 high-performance SACs that activate PMS more effectively could be designed.

726 **3.4. PDS activation**

727 Peroxydisulphate (PDS) is another type of persulfate that can be used to degrade
728 pollutants, which is more easily activated by energy transfer methods such as photolysis,
729 electrolysis or pyrolysis than PMS due to their lower bond dissociation energy [140].
730 Moreover, PDS is relatively less costly and toxic than PMS and is more inclusive of pH
731 conditions [141]. However, PDS has the problem of high concentration of SO_4^{2-} in
732 effluent water, and low utilization efficiency in AOPs [142, 143]. Unlike PMS, which
733 is more reactive and can be activated by a variety of carbon-based materials catalysts,

there are far fewer reports of SACs activation of PDS than PMS [144]. Considering the cost and oxidation capacity, SACs has great potential and space in the future research on AOP systems for activating PDS.

It has been reported that the production of Go-Fe(II) and Go-Fe(III) by the straightforward adsorption of iron ions on graphene oxide (GO) can increase the activity of PDS. In contrast, the iron loading of GO-Fe(III) (10.7 wt%) was higher than that of GO-Fe(II) (7.8 wt%) and the activation of PDS by GO-Fe(III) could degrade 97.3% of phenol within 600 min with a corresponding pseudo-first-order rate constant of 8×10^{-4} min^{-1}, indicating a better degradation rate than GO-Fe(II). Because GO-Fe(III) activates PDS more potently, Fe(III) on GO-Fe(III) may react with PDS to produce Fe(II) ions (Eq. (24)). The surface of PDS could then undergo a reaction with the released Fe(II) ions to release Fe(III) into the solution (Eq. (25)). The whole process could reduce Fe ion leaching, increase the consumption of PDS, and promote the production of free radicals (·OH, $SO_4^{\cdot-}$ and $O_2^{\cdot-}$) and $^1O_2$ [145]. In common Fe-based MOFs, Fe (III) induces PDS activation by single electron reduction with low reactivity [146]. Pu et al. assembled three ferrous based MOFs to improve the reactivity of PDS activation. All three Fe(II)-based MOFs with PDS were effective in degrading SMX, and the decomposition rate of SMX was bound up with the content of total Fe(II) active sites in the catalyst. The decomposition rate constant (K) of Fe(Nic) with the best degradation efficiency was 0.0566 min^{-1}. During the degradation process, PDS could be activated by atom-dispersed Fe(II) sites in Fe(II)-MOFs. The surface-bound Fe(II) (≡Fe(II)) provided available electrons to initiate free radical chain reactions, inducing

the formation of the major reactive species $SO_4^{\cdot -}$ and ·OH, as well as other reaction intermediates, which were the main activation pathway. In addition, Fe(III) and Fe(II) in aqueous solution could also induce partial homogenization processes involved in activation [51].

$$Fe^{3+} + S_2O_8^{2-} \rightarrow Fe^{2+} + S_2O_8^{\cdot -} \quad (24)$$

$$Fe^{2+} + S_2O_8^{2-} \rightarrow Fe^{3+} + SO_4^{\cdot -} + SO_4^{2-} \quad (25)$$

To improve the efficiency of PDS utilization, Jiang et al. reported an atomically dispersed Fe(III) with nitrogen-doped carbon (Fe-N-C), which could effectively activate PDS without generating free radicals. In order to selectively degrade the target pollutants, the atomically dispersed Fe(III) was linked with pyridine nitrogen atoms and transformed to Fe(V) by two-electron extraction of PDS. While the Fe_2O_3 particles displayed no activity, the PDS/Fe-N-C system significantly reduced the amount of 2,4-dichlorophenol (2,4-DCP), suggesting that granular Fe(III) oxide was inactive for activating PDS while atomically distributed Fe sites improved the reactivity. In contrast to the radical-based oxidation mechanism, it has been demonstrated that Fe(IV) and Fe(V) oxidize PMSO to form the respective sulfones by an oxygen transfer pathway [49]. Given that PDS oxidized the monatomic Fe(III) in Fe-N-C to create high-valence iron species and that PDS/Fe-N-C had roughly the same selectivity for contaminant degradation as Fe(V), Fe(V) may serve as an intermediary oxidant in the process of removing pollutants. The higher valence of Fe(V) utilized more of the oxidation capacity of PDS compared to free radical oxidation, providing a new route for selective destruction of specific organic contaminants by PDS activation.

A novel C_3N_4-rGO sandwich structure was designed to stabilize the dispersed single-atom Fe catalysts, which could avoid clumping of Fe atoms under extreme pH conditions and maintain good reactivity. The C_3N_4-Fe-rGO/PDS system could completely remove tetracycline (TC) within 15 min with a K value was 0.28 min^{-1}, which was 51.9, 21.5 and 3.5 times faster than g-C_3N_4, C_3N_4-rGO and C_3N_4-Fe, respectively. When C_3N_4-Fe was used as catalyst for the degradation of TC, ·OH and $SO_4^{\cdot-}$ free radicals were the main active species, and the contribution of $SO_4^{\cdot-}$ was greater than that of ·OH radical. Additionally, Fe atoms were proved as the main reaction sites. The sandwich structure of C_3N_4-Fe-rGO had a clear advantage over C_3N_4-Fe. It showed good catalytic efficiency in all pH ranges from 0 to 14, the reaction rate was significantly higher by a factor of 35 compared to C_3N_4-Fe at extreme pH values [53]. Wang et al. reported that a magnetic Fe-C/N composite with a carbon coating could degrade 98.11% of AR73 within 10 min by activating PDS. In the system of Fe-C/N/PS degradation of AR37, $SO_4^{\cdot-}$, ·OH and $^1O_2$ were produced simultaneously, with the non-radical degradation pathway of $^1O_2$ playing a major role. In Fe-C/N catalyst, the synergistic effect of Fe_3C and Fe_3N resulted in excellent performance [39]. Yang et al. synthesized Ni, Fe and N-tri-doped carbon catalysts (4Ni2Fe@20NAC), in which Fe oxides, Fe^0 and iron nitrogen complexes (FeN_x) were coexisting. The introduction of Ni led to the formation of more Fe^0, which improved the catalytic activity. N could coordinate Fe to generate FeN_x species and catalysts with more FeN_x sites also showed better catalytic activity and stability, as FeN_x was the active center of the catalyst. 4Ni2Fe@15NAC activated PDS showed higher removal efficiency for the

degradation of MO, generated by the adsorption of PDS of $SO_4^{\cdot-}$ and ·OH and a heterogeneous reaction between N species on the catalyst surface played a dominant role [36].

Table 2

Summary of the various carbon-based Fe-SACs for AOP applications

Catalyst (Usage amount, g·L^{-1})	Metal amount (wt%)	AOP applications	Pollutants	Removal efficiency	Pseudo-first-order rate (min^{-1})	Stability (Removal efficiency after recycling)	Major active species	Ref
Fe-NG/MCNS(0.2)	0.15	Photocatalytic	BPA	96% (120 min)	(-)	(-)	$\cdot O_2^-$ and ·OH	[37]
FeSAC-800(0.5)	(-)	photo/PMS	NOR	87.2% (60 min)	0.031	4 cycles, 85%	$\cdot O_2^-$ and $^1O_2$	[57]
I-FeNx/g-C_3N_4-5(0.5)	18.2	Photo/H_2O_2	MB	98.9% (11 min)	0.560	(-)	·OH	[85]
S-Fe/CN-4(0.5)	17.7	Photo/H_2O_2	MB	100% (5 min)	(-)	4 cycles, 98.8%	·OH	[35]
Fe-g-C_3N_4/GMC(0.8)	1.44	H_2O_2	AR 73	99.2% (40 min)	0.184	7 cycles, 90%	·OH	[38]
Fe_1-N_V/CN(-)	1.0	Photo/H_2O_2	CIP	91% (60 min)	0.048	(-)	·OH	[128]
U-g-PAO/Fe(0.1)	24.04	Photo/H_2O_2	OFX	99.4% (35 min)	0.56	5 cycles, 98%	·OH	[62]
Fe–CN/P(0.3)	7.0	Photo/H_2O_2	TCH	98.0% (60 min)	(-)	5 cycles, 91.3%	·OH	[61]
SAFe@HSC(-)	1.62	electro/H_2O_2	TAP	100% (40 min)	0.098	Continuous flow 6 h, 97.2%	·OH	[54]
Fe/N-DG(0.5)	2.77	electro/H_2O_2	CAP	97.6% (180 min)	(-)	5 cycles, 95.5%	$\cdot O_2^-$ and ·OH	[55]
AD-Fe/3DPC(-)	2.23	electro/H_2O_2	SMX	98% (40 min)	0.102	10 cycles, 98%	·OH	[46]
1.2Fe–N–C(0.15)	0.57	PMS	Phenol	97% (10 min)	0.331	4 cycles, 57%	$^1O_2$	[43]
Fe@COF(0.1)	2.14	PMS	Orange II	100% (45 min)	(-)	5 cycles, 91.2%	$^1O_2$	[139]
Fe SA/NPCs(0.5)	2.17	PMS	Rh B	100% (30 s)	19.657	(-)	$^1O_2$	[147]
Fe-N_4-PC-2(0.03)	1.23	PMS	SMX	100% (20 min)	(-)	4 cycles, 89%	$\cdot O_2^-$ and $^1O_2$	[50]
FeSA-NC(0.05)	2.45	PMS	PNP	99% (5 min)	0.302	3 cycles, 64%	$\cdot O_2^-$ and $^1O_2$	[86]
Fe^{III}-TAML(-)	(-)	PMS	4-CP	100% (9 min)	0.521	(-)	Fe(IV)=O	[48]
CNF(0.1)	3.46	PMS	4-CP	100% (20 min)	0.254	(-)	Fe(V)=O	[47]
Fe_{SA}-N-C(0.15)	3.92	PMS	BPA	100% (30 min)	0.240	3 cycles, 80%	Fe(IV)=O	[148]
SA Fe–g–C_3N_4(0.1)	4.07	PMS	TC	93.29% (40 min)	0.044	4 cycles, 91%	Fe(IV)=O and $^1O_2$	[52]
ISA-Fe/MC(0.05)	2.40	PMS	Phenol	100% (6 min)	1.096	3 cycles, 5%	$^1O_2$	[42]
Fe-N@C(0.1)	0.57	PMS	PCM	100% (20 min)	0.247	3 cycles, 100%	$\cdot O_2^-$ and $^1O_2$	[58]
Fe-N-C(0.1)	0.84	PMS	PCM	100% (40 min)	0.032	5 cycles, 80%	Fe(IV)=O and Fe(V)=O	[59]

FeCo@NC-1(0.1)	0.98	PMS	BPA	100% (1 min)	6.062	8 cycles, 80%	·OH, $SO_4^{\cdot-}$ and $^1O_2$	[44]
GO-Fe(III)(0.5)	10.7	PDS	Phenol	97.3% (600 min)	8×10^{-4}	4 cycles, 78.1%	·OH, $SO_4^{\cdot-}$ and $^1O_2$	[145]
Fe(II)MOFs(0.5)	(-)	PDS	SMX	97% (180 min)	0.057	(-)	·OH and $SO_4^{\cdot-}$	[51]
Fe(III)-N-C(0.2)	5.0	PDS	2,4-DCP	95% (90 min)	(-)	(-)	Fe(V)=O	[49]
C_3N_4-Fe-rGO(0.4)	5.0	PDS	TC	100% (15 min)	0.280	10 cycles, 99%	·OH and $SO_4^{\cdot-}$	[53]
Fe-C/N(1.0)	(-)	PDS	AR37	98.11% (10 min)	0.492	4 cycles, 92.99%	$^1O_2$	[39]
4Ni2Fe@20NAC	2.26	PDS	MO	89% (60 min)	0.023	5 cycles, 79.8%	·OH and $SO_4^{\cdot-}$	[36]

4. Catalyst stability

Most of the available carbon-based catalysts have a short lifetime in AOPs and the surface properties of the catalysts change with increasing reaction time. Therefore, the evaluation of catalyst stability is a key indicator for investigating potential applications of catalysts. In the report of Wang et al., the carbon-based catalyst (NPC) showed very poor stability in SMX degradation, while the stability of the catalyst (Fe-N_4-PC) was greatly improved with the introduction of iron atoms [50]. After three rounds of catalytic reactions, the adsorption efficiency of rhodamine B (Rh B) degraded by the FeSA/NPCs/PMS system decreased significantly. After a annealing treatment, the degradation and adsorption effect of FeSA/NPC catalyst were recovered and the amount of pyrrole N in the catalysts used increased significantly, so Yang et al. suggested that the adsorption of Rh B at the catalyst active site might be consistent with a “donor-acceptor” mechanism, where pyrrole N acted as an electron donor and Rh B acts as an electron acceptor [147].

The catalytic activity of Fe@COF prepared by Yao et al. decreased successively after use and the oxygen content of the catalyst increased from 8.06 at% to 11.66 at%.

During PMS activation, some Fe(II) centers in the catalyst underwent a valence change to form Fe(III), which resulted in an enhanced Fe(III) oxidation state on the surface of the used Fe@COF [139]. During PDS activation, the interlaminar structure of C_3N_4-rGo composites doped with a single atom of Fe could keep the iron sites from leaching away. The stability tests were carried out by Zuo et al. by recovering C_3N_4-Fe-rGo catalysts with different pH values, at pH=4, pH=0, pH= 7 and pH=14 conditions for four cycles (Fig. 10a). It was obvious that C_3N_4-Fe-rGo showed good recyclability and less loss of activity after the entire experimental cycle. The degradation efficiency of TC decreased by more than 50% after five cycles compared to C_3N_4-Fe. As the C_3N_4-Fe-rGO shown the least amount of Fe leaching from the intercalated structure, it demonstrated steady degrading efficiency during ten reaction cycles (Fig. 10b). The amount of residual iron in the catalyst did not vary significantly during the first five reaction cycles (Fig. 10c). Moreover, the bonding environment of the Fe atoms in C_3N_4-Fe-rGo was stable, and the reduction and oxidation potentials of Fe sites were basically unchanged after cycling the reaction [53].

The stability of Fe-N@C produced by the in-situ pyrolysis of *Enteromorpha* was tested by Chen et al. After three cycles, the removal rate k value of PCM degraded by activated PMS dropped from 0.1213 to 0.0556 min^{-1} (Fig. 10d). This can be attributed to the adsorption of PCM and the intermediates of PCM covering the surface sites and reducing the contact area between Fe-N@C and PMS. The PCM removal rate of used Fe-N@C can be restored to 0.1142 min^{-1} after thermal regeneration. The catalyst was structurally stable as shown in Fig. 10e. The fractions of π-π* shake up satellite C and

graphite N remained almost unchanged over the three cycles of the catalyst compared to the fresh sample. The used Fe-N@C Fe 2p, in comparison, only displayed a little fractional shift from Tet. Fe(III) to Oct. Fe (III) [58]. Similarly, the degradation performance of Fe-NC extracted from *Enteromorpha* gradually decreased with increasing number of cycles. The conversion of Fe species during the catalytic reaction also resulted in a decrease in catalyst activity, with a small proportion of the used catalyst being oxidized from Fe(II) to Fe(III) [57]. In the first three cycles of He et al., 1.2-Fe-N-C could completely degrade phenol by activating PMS, but in the fourth cycle experiment, the removal efficiency decreased at a drastic rate. After four cycles, the O content in 1.2-Fe-N-C grew dramatically from 7.81 at% to 14.53 at%. Subsequently, the doped N partially was then oxidized, and the FeN_x sites that were on the surface of the catalyst were destroyed. They suggested that the durability and stability of the catalyst could be improved by designing a carbon shell to protect the FeN_x sites [43].

In conclusion, most of the carbon-based single iron atom catalysts reported so far were somewhat more stable than conventional carbon-based catalysts. The stability of Fe-SACs was mainly influenced by the amount of Fe leached from the catalyst, the consumption of pyrrole N and the catalytic sites covered during the degradation of the contaminant [42]. Although most Fe-SACs could recover their degradation performance after a few cycles and then be reused by simple treatment, some losses were unavoidable during catalyst remediation and the catalyst activity gradually decreased with increasing number of cycles. In the future design of Fe-SACs, both the catalytic performance and the recycle ability of the catalyst need to be improved.

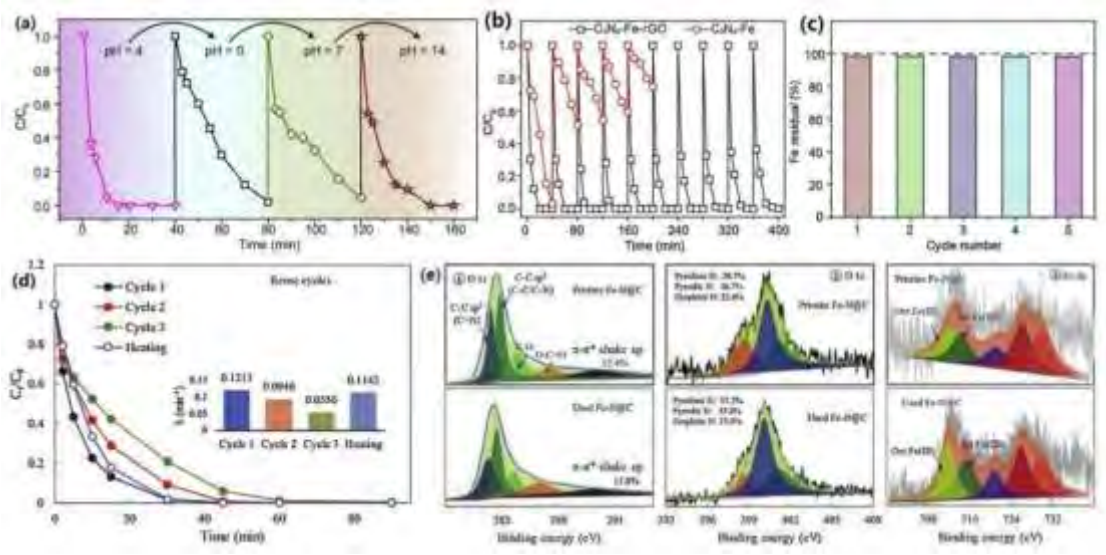

Fig. 10(a)The degradation performance during cycles of solution with different pH conditions; (b) Cycles of tetracycline degradation experiment performance; (c) Fe mass ratio in the catalyst after each round [53]. (d)Reuse cycles of Fe-N@C 700 for PCM; (e) ①O 1 s; ②N 1 s; ③Fe 2p of fresh Fe-N@C and used Fe-N@C [58].

5. Conclusion and perspectives

A link between homogeneous and heterogeneous catalysis has been created by the discovery and development of SACs. Carbon-based SACs have been reported to exhibit excellent catalytic activity for a variety of difficult organic compounds in wastewater treatment. Because of its high density of FeN_x active sites and high catalytic performance, carbon-based Fe-SACs have become a popular target in the direction of SACs and have been explored in many experiments. In this review, the synthetic strategies and environmental applications of Fe-SACs in recent years were summarized, focusing on the application and mechanisms of Fe-SACs via AOPs for refractory organic compounds in water. Pyrolysis strategy using MOFs, polymer, small molecule organic matter and biomass as precursors was the most commonly used method for the synthesis of carbon-based Fe-SACs. In addition, wet impregnation, physical and

chemical deposition and ball milling have also been used for the synthesis of carbon-based Fe-SACs. SACs have the highest atomic efficiency and excellent structure and electron transfer ability, which can induce various non-radical and radical reactions in AOPs applications. In non-radical processes, the ROS formed by Fe-SACs are more selective towards organic molecules with high electron densities. Therefore, the free radical and non-free radical systems catalyzed by carbon-based Fe-SACs were expected to achieve both rapid oxidation and deep mineralization followed by selective removal of the target pollutants from the wastewater.

An increasing number of studies have been carried out on carbon-based SACs. Despite the excellent performance of Fe-SACs in environmental applications, significant challenges and opportunities remain in the research related to their synthesis and application.

(1) Multiple synthetic constraints

At present, most syntheses of Fe-SACs required the selection of specific carriers by high temperature pyrolysis. However, the mechanism of SACs formation and the structure-catalytic relationship during thermal transformation were not fully understood, and the synthesis process often required repeated experiments, resulting in material and energy consumption, as well as time and cost wastage. Furthermore, although some reports have investigated general synthetic strategies for SACs, general studies on the preparation and utilization of SAC using a single metal on a single carrier or using multiple metals on a single carrier remain to be carried out.

(2) The loading of Fe atoms in SACs

904 The density of FeN_x active sites may be directly impacted by the metal loading in
905 Fe-SACs, and a moderate increase in the number of monoatomic sites could greatly
906 improve the catalytic activity of SACs in AOPs. However, an overabundance of metal
907 atom loading would combine into nanoparticles, invariably cause metal leaching, and
908 perhaps cause secondary contamination. Therefore, most of the existing Fe-SACs carry
909 less than 5 wt% of metal, and research on how to increase the density and stability of
910 individual iron atoms on the carbon base would require further exploration.
911 (3) Precise adjustment of the coordination environment
912 The coordination number and coordination environment of the single-atom active
913 center largely determined its electronic properties and the corresponding catalytic
914 performance. Strategies to accurately control the coordination geometry and the
915 number of isolated atoms in the reaction center by adding heteroatoms, vacancies, and
916 structural flaws to the carbon matrix still needed to be developed.
917 (4) Identification of potential active sites
918 Currently, it was possible to observe individual atoms using the HADDF-STEM
919 technique and to determine their coordination structures by XAS analysis. However, a
920 robust characterization technique that could directly detect the coordination structure
921 and electronic properties of individual atomic positions in SACs was still lacking.
922 Different compositions of carbon substrates bound to iron single atoms could trigger
923 multiple radical/non-radical pathways, and the single-atom catalytic sites in different
924 coordination environments might differ under actual catalytic conditions.
925 (5) The real wastewater applications

In the real wastewater environment, there are many complex background components such as heavy metals, inorganic salts, organic compounds and pathogenic microorganisms in addition to the target pollutants. These background components can destroy the carbon matrix, and then affect the catalyst activity and stability of carbon-based Fe-SACs. In order to maintain the overall performance of catalyst in practical application of AOPs, it is vital to choose appropriate metal precursors and carriers prior to synthesis. In existing studies, the sandwich structure of atom-dispersed Fe sites on the g-C_3N_4 carrier is stabilized by introducing a layer of rGO, which seems to have the best stability of Fe-SACs.

Conflicts of interest

There are no conflicts of interest to declare.

Acknowledgements

This study was financially supported by the Program for the National Natural Science Foundation of China (U20A20323, 52100180, 52100182), the Program for Changjiang Scholars and Innovative Research Team in University (IRT-13R17), the Fundamental Research Funds for the Central Universities (531119200086, 531118010114, 541109060031, 531118010574), and the China National Postdoctoral Program for Innovative Talents (BX20200119), the Project funded by China Postdoctoral Science Foundation (2021M690904, 2021M700041), the Natural Science Foundation of Hunan Province, China (2022JJ40086).

References

[1] P. Gautam, S. Kumar, S. Lokhandwala, Journal of Cleaner Production, 237 (2019) 117639.

[2] Y. Liang, Y. Zeng, X. Tang, W. Xia, B. Song, F. Yao, Y. Yang, Y. Chen, C. Peng, C. Zhou, C. Lai, Chemical Engineering Journal, 451 (2023) 138936.

[3] K. Silas, W. Ghani, T.S.Y. Choong, U. Rashid, Catalysts, 10 (2020) 25.

[4] B. Song, J. Gong, W. Tang, G. Zeng, M. Chen, P. Xu, M. Shen, S. Ye, H. Feng, C. Zhou, Y. Yang, Science of The Total Environment, 713 (2020) 136645.

[5] C.W. Jones, Acs Catalysis, 8 (2018) 10913-10913.

[6] C. Wen, A.Y. Yin, W.L. Dai, Applied Catalysis B-Environmental, 160 (2014) 730-741.

[7] M.C. Shen, Y.X. Zhang, Y. Zhu, B. Song, G.M. Zeng, D.F. Hu, X.F. Wen, X.Y. Ren, Environmental Pollution, 252 (2019) 511-521.

[8] Y. Fu, Z. Yin, L. Qin, D. Huang, H. Yi, X. Liu, S. Liu, M. Zhang, B. Li, L. Li, W. Wang, X. Zhou, Y. Li, G. Zeng, C. Lai, Journal of Hazardous Materials, 422 (2022) 126950.

[9] Z. Wu, Y. Wang, Z. Xiong, Z. Ao, S. Pu, G. Yao, B. Lai, Applied Catalysis B: Environmental, 277 (2020) 119136.

[10] Y. Li, T. Yang, S. Qiu, W. Lin, J. Yan, S. Fan, Q. Zhou, Chemical Engineering Journal, 389 (2020) 124382.

[11] J. Xu, H. Olvera-Vargas, B.J.H. Loh, O. Lefebvre, Applied Catalysis B: Environmental, 271 (2020) 118923.

[12] V.I. Parvulescu, I. Fechete, Catalysis Today, 306 (2018) 1-1.

[13] K.S. Sindhu, S.M. Ujwaldev, K.K. Krishnan, G. Anilkumar, Journal of Catalysis, 348 (2017) 146-150.

[14] Z. Xu, Z. Ao, M. Yang, S. Wang, Journal of Hazardous Materials, 424 (2022) 127427.

[15] T.A. Bender, J.A. Dabrowski, M.R. Gagne, Nature Reviews Chemistry, 2 (2018) 35-46.

[16] K. Sordakis, C.H. Tang, L.K. Vogt, H. Junge, P.J. Dyson, M. Beller, G. Laurenczy, Chemical Reviews, 118 (2018) 372-433.

[17] B. Huang, Z. Wu, H. Zhou, J. Li, C. Zhou, Z. Xiong, Z. Pan, G. Yao, B. Lai, J Hazard Mater, 412 (2021) 125253.

[18] C.C. Hou, H.F. Wang, C.X. Li, Q. Xu, Energy & Environmental Science, 13 (2020) 1658-1693.

[19] B.T. Qiao, A.Q. Wang, X.F. Yang, L.F. Allard, Z. Jiang, Y.T. Cui, J.Y. Liu, J. Li, T. Zhang, Nature Chemistry, 3 (2011) 634-641.

[20] F. Chen, X.Z. Jiang, L.L. Zhang, R. Lang, B.T. Qiao, Chinese Journal of Catalysis, 39 (2018) 893-898.

[21] M.B. Gawande, P. Fornasiero, R. Zboril, Acs Catalysis, 10 (2020) 2231-2259.

[22] J.Y. Liu, Current Opinion in Green and Sustainable Chemistry, 22 (2020) 54-64.

[23] N.Q. Zhang, C.L. Ye, H. Yan, L.C. Li, H. He, D.S. Wang, Y.D. Li, Nano Research, 13 (2020) 3165-3182.

[24] R. Lang, W. Xi, J.-C. Liu, Y.-T. Cui, T. Li, A.F. Lee, F. Chen, Y. Chen, L. Li, L. Li, J. Lin, S. Miao, X. Liu, A.-Q. Wang, X. Wang, J. Luo, B. Qiao, J. Li, T. Zhang, Nature Communications, 10 (2019) 234.

[25] M.B. Gawande, P.S. Branco, R.S. Varma, Chemical Society Reviews, 42 (2013) 3371-3393.

[26] P. Duan, X. Liu, B. Liu, M. Akram, Y. Li, J. Pan, Q. Yue, B. Gao, X. Xu, Applied Catalysis B: Environmental, 298 (2021) 120532.

[27] B. Singh, M.B. Gawande, A.D. Kute, R.S. Varma, P. Fornasiero, P. McNeice, R.V. Jagadeesh, M. Beller, R. Zboril, Chemical Reviews, 121 (2021) 13620-13697.

[28] A.Q. Wang, J. Li, T. Zhang, Nature Reviews Chemistry, 2 (2018) 65-81.

[29] X. Li, X. Yang, Y. Huang, T. Zhang, B. Liu, Advanced Materials, 31 (2019) 1902031.

[30] L. Jiao, H.Y. Yan, Y. Wu, W.L. Gu, C.Z. Zhu, D. Du, Y.H. Lin, Angewandte Chemie-International Edition, 59 (2020) 2565-2576.
[31] J. Xi, H.S. Jung, Y. Xu, F. Xiao, J.W. Bae, S. Wang, Advanced Functional Materials, 31 (2021) 2008318.
[32] C.X. Zhao, B.Q. Li, J.N. Liu, Q. Zhang, Angewandte Chemie-International Edition, 60 (2021) 4448-4463.
[33] D. Yu, L. Wang, T. Yang, G. Yang, D. Wang, H. Ni, M. Wu, Chemical Engineering Journal, 404 (2021) 127075.
[34] J. Gao, Y. Wang, S. Zhou, W. Lin, Y. Kong, ChemCatChem, 9 (2017) 1708-1715.
[35] S. An, G. Zhang, J. Liu, K. Li, G. Wan, Y. Liang, D. Ji, J.T. Miller, C. Song, W. Liu, Z. Liu, X. Guo, Chinese Journal of Catalysis, 41 (2020) 1198-1207.
[36] G. Yang, J. Dong, B. Xing, S. Mo, X. Song, X. Liu, J. Yuan, Separation and Purification Technology, 252 (2020) 117440.
[37] J. Liu, B. Wang, J. Huang, R. Yang, R. Wang, Y. Song, C. Wang, Y. Hua, H. Xu, H. Li, Colloids and Surfaces A: Physicochemical and Engineering Aspects, 629 (2021) 127360.
[38] J.Q. Ma, Q.F. Yang, Y.Z. Wen, W.P. Liu, Applied Catalysis B-Environmental, 201 (2017) 232-240.
[39] C. Wang, Q.Q. Yang, Z.H. Li, K.Y.A. Lin, S.P. Tong, Separation and Purification Technology, 213 (2019) 447-455.
[40] L. Yang, H. Yang, S. Yin, X. Wang, M. Xu, G. Lu, Z. Liu, H. Sun, Small, 18 (2022) 2104941.
[41] L. Ma, S. Chen, Z. Pei, Y. Huang, G. Liang, F. Mo, Q. Yang, J. Su, Y. Gao, J.A. Zapien, C. Zhi, ACS Nano, 12 (2018) 1949-1958.
[42] Z.Q. Li, K. Li, S.L. Ma, B.J. Dang, Y. Li, H.C. Fu, J. Du, S.X. Meng, Journal of Colloid and Interface Science, 582 (2021) 598-609.
[43] J. He, Y. Wan, W. Zhou, J Hazard Mater, 405 (2021) 124199.
[44] J. Yang, D. Zeng, J. Li, L. Dong, W.-J. Ong, H. He, Chemical Engineering Journal, 404 (2021) 126376.
[45] S. Tonda, S. Kumar, S. Kandula, V. Shanker, Journal of Materials Chemistry A, 2 (2014) 6772-6780.
[46] P. Cao, X. Quan, K. Zhao, S. Chen, H. Yu, Y. Su, Environ Sci Technol, 54 (2020) 12662-12672.
[47] H. Li, C. Shan, B. Pan, Environ Sci Technol, 52 (2018) 2197-2205.
[48] H. Li, C. Shan, W. Li, B. Pan, Water Res, 147 (2018) 233-241.
[49] N. Jiang, H. Xu, L. Wang, J. Jiang, T. Zhang, Environ Sci Technol, 54 (2020) 14057-14065.
[50] J. Wang, B. Li, Y. Li, X. Fan, T. Zhang, G. Zhang, W. Peng, Advanced Science, 8 (2021) 2101824.
[51] M. Pu, J. Niu, M.L. Brusseau, Y. Sun, C. Zhou, S. Deng, J. Wan, Chemical Engineering Journal, 394 (2020) 125044.
[52] X. Peng, J. Wu, Z. Zhao, X. Wang, H. Dai, L. Xu, G. Xu, Y. Jian, F. Hu, Chemical Engineering Journal, 427 (2022) 130803.
[53] S. Zuo, X. Jin, X. Wang, Y. Lu, Q. Zhu, J. Wang, W. Liu, Y. Du, J. Wang, Applied Catalysis B: Environmental, 282 (2021) 119551.
[54] D. Zhang, K. Yin, Y. Tang, Y. Wei, H. Tang, Y. Du, H. Liu, Y. Chen, C. Liu, Chemical Engineering Journal, 427 (2022) 130996.
[55] X. Song, H. Zhang, Z. Bian, H. Wang, Journal of Hazardous Materials, 412 (2021) 125162.
[56] T. Hou, H. Peng, Y. Xin, S. Wang, W. Zhu, L. Chen, Y. Yao, W. Zhang, S. Liang, L. Wang, ACS Catalysis, 10 (2020) 5502-5510.
[57] X. Li, K. Hu, Y. Huang, Q. Gu, Y. Chen, B. Yang, R. Qiu, W. Luo, B.M. Weckhuysen, K. Yan, Journal of Energy Chemistry, 69 (2022) 282-291.

[58] C. Chen, T.F. Ma, Y.N. Shang, B.Y. Gao, B. Jin, H.B. Dan, Q. Li, Q.Y. Yue, Y.W. Li, Y. Wang, X. Xu, Applied Catalysis B-Environmental, 250 (2019) 382-395.
[59] L. Peng, X. Duan, Y. Shang, B. Gao, X. Xu, Applied Catalysis B: Environmental, 287 (2021) 119963.
[60] Z. Zhao, W. Zhang, W. Liu, Y. Li, J. Ye, J. Liang, M. Tong, Chemical Engineering Journal, 407 (2021) 127167.
[61] S. Mao, C. Liu, Y. Wu, M. Xia, F. Wang, Chemosphere, 291 (2022) 133039.
[62] L. Mu, M. Wang, F. Jiang, Q. Gao, M. Zhang, Z. Xiong, Y. Li, R. Shen, J. Hu, G. Wu, Applied Catalysis B: Environmental, 298 (2021) 120574.
[63] K. Zhao, X. Quan, Y. Su, X. Qin, S. Chen, H. Yu, Environ Sci Technol, 55 (2021) 14194-14203.
[64] Z.-H. Xue, D. Luan, H. Zhang, X.W. Lou, Joule, 6 (2022) 92-133.
[65] C. Gao, J. Low, R. Long, T. Kong, J. Zhu, Y. Xiong, Chem Rev, 120 (2020) 12175-12216.
[66] C. Lu, R. Fang, X. Chen, Advanced Materials, 32 (2020) 1906548.
[67] Q. Zhang, J. Guan, Advanced Functional Materials, 30 (2020) 2000768.
[68] Y. Shang, X. Xu, B. Gao, S. Wang, X. Duan, Chem Soc Rev, 50 (2021) 5281-5322.
[69] B. Huang, Z. Wu, H. Zhou, J. Li, C. Zhou, Z. Xiong, Z. Pan, G. Yao, B. Lai, Journal of Hazardous Materials, 412 (2021) 125253.
[70] L. Jiao, H.L. Jiang, Chem, 5 (2019) 786-804.
[71] Y. Su, M.C. Lu, R.D. Su, W.Z. Zhou, X. Xu, Q. Li, Chin. Chem. Lett., 33 (2022) 2573-2578.
[72] Y.S. Wei, M. Zhang, R. Zou, Q. Xu, Chem Rev, 120 (2020) 12089-12174.
[73] A. Han, B. Wang, A. Kumar, Y. Qin, J. Jin, X. Wang, C. Yang, B. Dong, Y. Jia, J. Liu, X. Sun, Small Methods, 3 (2019) 1800471.
[74] S. Fu, C. Zhu, D. Su, J. Song, S. Yao, S. Feng, M.H. Engelhard, D. Du, Y. Lin, Small, 14 (2018) 1703118.
[75] L. Jiao, G. Wan, R. Zhang, H. Zhou, S.H. Yu, H.L. Jiang, Angewandte Chemie-International Edition, 57 (2018) 8525-8529.
[76] H. Zhang, S. Hwang, M. Wang, Z. Feng, S. Karakalos, L. Luo, Z. Qiao, X. Xie, C. Wang, D. Su, Y. Shao, G. Wu, J Am Chem Soc, 139 (2017) 14143-14149.
[77] Y. Chen, S. Ji, Y. Wang, J. Dong, W. Chen, Z. Li, R. Shen, L. Zheng, Z. Zhuang, D. Wang, Y. Li, Angew Chem Int Ed Engl, 56 (2017) 6937-6941.
[78] X. Chen, D.-D. Ma, B. Chen, K. Zhang, R. Zou, X.-T. Wu, Q.-L. Zhu, Applied Catalysis B: Environmental, 267 (2020) 118720.
[79] L. Jiao, J.T. Zhu, Y. Zhang, W.J. Yang, S.Y. Zhou, A.W. Li, C.F. Xie, X.S. Zheng, W. Zhou, S.H. Yu, H.L. Jiang, Journal of the American Chemical Society, 143 (2021) 19417-19424.
[80] R. Jiang, L. Li, T. Sheng, G. Hu, Y. Chen, L. Wang, J Am Chem Soc, 140 (2018) 11594-11598.
[81] Y. Ye, F. Cai, H. Li, H. Wu, G. Wang, Y. Li, S. Miao, S. Xie, R. Si, J. Wang, X. Bao, Nano Energy, 38 (2017) 281-289.
[82] D. Tenne, B. Bogoslavsky, A. Bino, European Journal of Inorganic Chemistry, 2015 (2015) 4159-4161.
[83] K. Kim, T. Kang, M. Kim, J. Kim, Applied Catalysis B-Environmental, 275 (2020) 9.
[84] C. Du, Y. Gao, J. Wang, W. Chen, Journal of Materials Chemistry A, 8 (2020) 9981-9990.
[85] S.F. An, G.H. Zhang, T.W. Wang, W.N. Zhan, K.Y. Li, C.S. Song, J.T. Miller, S. Miao, J.H. Wang, X.W. Guo, Acs Nano, 12 (2018) 9441-9450.
[86] Z.Y. Du, J.X. Qin, K. Zhang, L.W. Jia, K. Tian, J.F. Zhang, H.J. Xie, Applied Surface Science, 591 (2022) 10.
[87] Y. Xiong, W.M. Sun, P.Y. Xin, W.X. Chen, X.S. Zheng, W.S. Yan, L.R. Zheng, J.C. Dong, J. Zhang, D.S. Wang, Y.D. Li, Advanced Materials, 32 (2020) 8.

[88] A. Zitolo, V. Goellner, V. Armel, M.T. Sougrati, T. Mineva, L. Stievano, E. Fonda, F. Jaouen, Nat Mater, 14 (2015) 937-942.
[89] H.Z. Yang, L. Shang, Q.H. Zhang, R. Shi, G.I.N. Waterhouse, L. Gu, T.R. Zhang, Nature Communications, 10 (2019) 9.
[90] L. Zhao, Y. Zhang, L.B. Huang, X.Z. Liu, Q.H. Zhang, C. He, Z.Y. Wu, L.J. Zhang, J.P. Wu, W.L. Yang, L. Gu, J.S. Hu, L.J. Wan, Nature Communications, 10 (2019) 11.
[91] J.L. Feng, M.L. Dou, Z.P. Zhang, F. Wang, Acs Applied Materials & Interfaces, 10 (2018) 37079-37086.
[92] H. Zhou, S. Hong, H. Zhang, Y.T. Chen, H.H. Xu, X.K. Wang, Z. Jiang, S.L. Chen, Y. Liu, Applied Catalysis B-Environmental, 256 (2019) 10.
[93] Y. Li, S.M. Zhu, Q.L. Liu, Z.X. Chen, J.J. Gu, C.L. Zhu, T. Lu, D. Zhang, J. Ma, Water Research, 47 (2013) 4188-4197.
[94] W. Xia, B. Song, H. Yi, E. Almatrafi, Y. Yang, Y. Fu, X. Huo, F. Qin, L. Xiang, Y. Zeng, G. Zeng, C. Zhou, Journal of Cleaner Production, 373 (2022) 133750 (2022).
[95] Y. Wang, B. Yu, K. Liu, X. Yang, M. Liu, T.-S. Chan, X. Qiu, J. Li, W. Li, Journal of Materials Chemistry A, 8 (2020) 2131-2139.
[96] C. Zhou, Y. Liang, W. Xia, E. Almatrafi, B. Song, Z. Wang, Y. Zeng, Y. Yang, Y. Shang, C. Wang, G. Zeng, Journal of hazardous materials, 441 (2022) 129871.
[97] Y. Lei, F. Yang, H. Xie, Y. Lei, X. Liu, Y. Si, H. Wang, Journal of Materials Chemistry A, 8 (2020) 20629-20636.
[98] X. Wang, J. Du, Q. Zhang, L. Gu, L. Cao, H.-P. Liang, Carbon, 157 (2020) 614-621.
[99] T. He, Y. Zhang, Y. Chen, Z. Zhang, H. Wang, Y. Hu, M. Liu, C.-W. Pao, J.-L. Chen, L.Y. Chang, Z. Sun, J. Xiang, Y. Zhang, S. Chen, Journal of Materials Chemistry A, 7 (2019) 20840-20846.
[100] Z.P. Zhang, X.J. Gao, M.L. Dou, J. Ji, F. Wang, Small, 13 (2017) 8.
[101] X.L. Wang, Y.P. Tong, G.D. Fang, Current Opinion in Chemical Engineering, 34 (2021) 7.
[102] K.W. Mou, Z.P. Chen, X.X. Zhang, M.Y. Jia, X.P. Zhang, X. Ge, W. Zhang, L.C. Liu, Small, 15 (2019) 8.
[103] H. Fei, J. Dong, Y. Feng, C.S. Allen, C. Wan, B. Volosskiy, M. Li, Z. Zhao, Y. Wang, H. Sun, P. An, W. Chen, Z. Guo, C. Lee, D. Chen, I. Shakir, M. Liu, T. Hu, Y. Li, A.I. Kirkland, X. Duan, Y. Huang, Nature Catalysis, 1 (2018) 63-72.
[104] J. Hamalainen, M. Ritala, M. Leskela, Chemistry of Materials, 26 (2014) 786-801.
[105] N.C. Cheng, X.L. Sun, Chinese Journal of Catalysis, 38 (2017) 1508-1514.
[106] X.F. Wang, B.T. Jin, Y. Jin, T.P. Wu, L. Ma, X.H. Liang, Acs Applied Nano Materials, 3 (2020) 2867-2874.
[107] Z.Y. Cai, B.L. Liu, X.L. Zou, H.M. Cheng, Chemical Reviews, 118 (2018) 6091-6133.
[108] S. Immohr, M. Felderhoff, C. Weidenthaler, F. Schuth, Angewandte Chemie-International Edition, 52 (2013) 12688-12691.
[109] I.Y. Jeon, Y.R. Shin, G.J. Sohn, H.J. Choi, S.Y. Bae, J. Mahmood, S.M. Jung, J.M. Seo, M.J. Kim, D.W. Chang, L.M. Dai, J.B. Baek, Proceedings of the National Academy of Sciences of the United States of America, 109 (2012) 5588-5593.
[110] X.G. Guo, G.Z. Fang, G. Li, H. Ma, H.J. Fan, L. Yu, C. Ma, X. Wu, D.H. Deng, M.M. Wei, D.L. Tan, R. Si, S. Zhang, J.Q. Li, L.T. Sun, Z.C. Tang, X.L. Pan, X.H. Bao, Science, 344 (2014) 616-619.
[111] D.H. Deng, X.Q. Chen, L. Yu, X. Wu, Q.F. Liu, Y. Liu, H.X. Yang, H.F. Tian, Y.F. Hu, P.P. Du, R. Si, J.H. Wang, X.J. Cui, H.B. Li, J.P. Xiao, T. Xu, J. Deng, F. Yang, P.N. Duchesne, P. Zhang, J.G. Zhou, L.T. Sun, J.Q. Li, X.L. Pan, X.H. Bao, Science Advances, 1 (2015) 9.

[112] K. Qian, H. Chen, W.L. Li, Z.M. Ao, Y.N. Wu, X.H. Guan, Environmental Science & Technology, 55 (2021) 7034-7043.
[113] L.T. Ma, S.M. Chen, Z.X. Pei, Y. Huang, G.J. Liang, F.N. Mo, Q. Yang, J. Su, Y.H. Gao, J.A. Zapien, C.Y. Zhi, Acs Nano, 12 (2018) 1949-1958.
[114] C. Du, Y.J. Gao, J.G. Wang, W. Chen, Journal of Materials Chemistry A, 8 (2020) 9981-9990.
[115] X.Q. Chen, L. Yu, S.H. Wang, D.H. Deng, X.H. Bao, Nano Energy, 32 (2017) 353-358.
[116] Q. Wang, K. Domen, Chemical Reviews, 120 (2020) 919-985.
[117] Y. Okada, K. Chiba, Chemical Reviews, 118 (2018) 4592-4630.
[118] S. Kundu, A. Patra, Chemical Reviews, 117 (2017) 712-757.
[119] C.Y. Zhou, E. Almatrafi, X.F. Tang, B.B. Shao, W. Xia, B. Song, W.P. Xiong, W.J. Wang, H. Guo, S. Chen, G.M. Zeng, Separation and Purification Technology, 286 (2022) 10.
[120] Y. Oh, J.O. Hwang, E.S. Lee, M. Yoon, V.D. Le, Y.H. Kim, D.H. Kim, S.O. Kim, ACS Appl Mater Interfaces, 8 (2016) 25438-25443.
[121] H.B. Cao, J. Wang, J.H. Kim, Z. Guo, J.D. Xiao, J. Yang, J.J. Chang, Y.C. Shi, Y.B. Xie, Applied Catalysis B-Environmental, 296 (2021) 12.
[122] E. Neyens, J. Baeyens, Journal of Hazardous Materials, 98 (2003) 33-50.
[123] S. Wang, Dyes and Pigments, 76 (2008) 714-720.
[124] J. Li, Q.Q. Ji, B. Lai, D.H. Yuan, Journal of the Taiwan Institute of Chemical Engineers, 80 (2017) 686-694.
[125] C. Gao, S. Chen, X. Quan, H. Yu, Y. Zhang, Journal of Catalysis, 356 (2017) 125-132.
[126] Y.P. Zhu, R.L. Zhu, Y.F. Xi, J.X. Zhu, G.Q. Zhu, H.P. He, Applied Catalysis B-Environmental, 255 (2019) 16.
[127] W.P. Kwan, B.M. Voelker, Environmental Science & Technology, 36 (2002) 1467-1476.
[128] L.N. Su, P.F. Wang, X.L. Ma, J.H. Wang, S.H. Zhan, Angewandte Chemie-International Edition, 60 (2021) 21261-21266.
[129] E. Brillas, I. Sires, M.A. Oturan, Chemical Reviews, 109 (2009) 6570-6631.
[130] C.H. Wang, J. Kim, V. Malgras, J. Na, J. Lin, J. You, M. Zhang, J.S. Li, Y. Yamauchi, Small, 15 (2019) 21.
[131] C. He, W. Xia, C.Y. Zhou, D.L. Huang, C. Zhang, B. Song, Y. Yang, J. Li, X. Xu, Y.N. Shang, L. Du, Chemical Engineering Journal, 430 (2022) 11.
[132] P.J. Duan, X.N. Liu, B.H. Liu, M. Akram, Y.W. Li, J.W. Pan, Q.Y. Yue, B.Y. Gao, X. Xu, Applied Catalysis B-Environmental, 298 (2021) 10.
[133] W.D. Oh, Z.L. Dong, T.T. Lim, Applied Catalysis B-Environmental, 194 (2016) 169-201.
[134] M.X. Yang, Z.X. Hou, X. Zhang, B.Y. Gao, Y.W. Li, Y.A. Shang, Q.Y. Yue, X.G. Duan, X. Xu, Environmental Science & Technology, 11.
[135] T. Zeng, S.Q. Li, J.A. Hua, Z.Q. He, X.L. Zhang, H.R. Feng, S. Song, Science of the Total Environment, 645 (2018) 550-559.
[136] X. Cheng, H.G. Guo, Y.L. Zhang, X. Wu, Y. Liu, Water Research, 113 (2017) 80-88.
[137] S.S.A. Shah, T. Najam, M.K. Aslam, M. Ashfaq, M.M. Rahman, K. Wang, P. Tsiakaras, S.Q. Song, Y. Wang, Applied Catalysis B-Environmental, 268 (2020) 20.
[138] Q. Lai, L. Zheng, Y. Liang, J. He, J. Zhao, J. Chen, ACS Catalysis, 7 (2017) 1655-1663.
[139] Y.J. Yao, H.Y. Yin, M.X. Gao, Y. Hu, H.H. Hu, M.J. Yu, S.B. Wang, Chemical Engineering Science, 209 (2019) 13.

[140] S. Waclawek, H.V. Lutze, K. Grubel, V.V.T. Padil, M. Cernik, D.D. Dionysiou, Chemical Engineering Journal, 330 (2017) 44-62.
[141] L.Z. Huang, X.L. Wei, E.L. Gao, C.B. Zhang, X.M. Hu, Y.Q. Chen, Z.Z. Liu, N. Finck, J. Lutzenkirchen, D.D. Dionysiou, Applied Catalysis B-Environmental, 268 (2020) 12.
[142] Y. Xue, N.N.T. Pham, G. Nam, J. Choi, Y.Y. Ahn, H. Lee, J. Jung, S.G. Lee, J. Lee, Chemical Engineering Journal, 408 (2021) 12.
[143] Y.A. Shang, X.N. Liu, Y.W. Li, Y. Gao, B.Y. Gao, X. Xu, Q.Y. Yue, Chemical Engineering Journal, 446 (2022) 12.
[144] X.G. Duan, H.Q. Sun, Z.P. Shao, S.B. Wang, Applied Catalysis B-Environmental, 224 (2018) 973-982.
[145] Y.G. Kang, H.C. Vu, Y.Y. Chang, Y.S. Chang, Chemical Engineering Journal, 387 (2020) 8.
[146] H.Z. Liu, T.A. Bruton, W. Li, J. Van Buren, C. Prasse, F.M. Doyle, D.L. Sedlak, Environmental Science & Technology, 50 (2016) 890-898.
[147] L.X. Yang, H.Q. Yang, S.Y. Yin, X.Y. Wang, M.W. Xu, G.L. Lu, Z.N. Liu, H. Sun, Small, 18 (2022) 14.
[148] Y. Li, T. Yang, S.H. Qiu, W.Q. Lin, J.T. Yan, S.S. Fan, Q. Zhou, Chemical Engineering Journal, 389 (2020) 10.